

New Ruthenium(II) Polypyridyl Compounds with Quinoline Type Ligands for the Treatment of Cutaneous Leishmaniasis

THESIS

Presented in Partial Fulfillment of the Requirements for the Degree Master of Science in
the Graduate School of The Ohio State University

By

Alba Pilar Evans, B.S.

Graduate Program in Chemistry

The Ohio State University

2017

Master's Examination Committee:

Dr. Claudia Turro, Advisor

Dr. James Cowan

Copyrighted by

Alba Pilar Evans

2017

Abstract

Cutaneous leishmaniasis (CL) is the most common form of the neglected tropical disease leishmaniasis, causing skin lesions and ulcers on exposed parts of the body often leaving life-long scars and serious disability. This disease is caused by protozoan *Leishmania* parasites that are transmitted via the bite of infected female *phlebotomine* sandflies, a species native to tropical regions. With 0.7-1.3 million new annual cases worldwide researchers are investigating new ways of combatting the illness before it progresses to its lethal forms. Photochemical therapy (PCT), more generally known as photodynamic therapy (PDT), has recently become an attractive mode of treatment in various medical fields due to the affordability and efficiency of new light sources and its low invasiveness. Ru(II)-polypyridyl complexes possess a unique combination of chemical stability in solution, strong absorption throughout the UV-vis light regions, and long excited state lifetimes, making them important contributors to this field. Ruthenium complexes containing monodentate N-heterocyclic aromatic ligand and a distortion of the pseudo-octahedral geometry have been shown to undergo ligand dissociation upon irradiation via the population of the metal-centered ligand field (3LF) state from the excited triplet metal-to-ligand charge transfer (3MLCT) state. This presents a mode of photoinduced target drug delivery that can be used to kill the parasites inside the CL infected cells. The following new complexes were synthesized and characterized using ESI-MS and NMR spectroscopy, $[Ru(tpy)(bpy)(Q)][PF_6]_2$ and $[Ru(tpy)(bpy)(CQ)][PF_6]_2$

(tpy = 2,2':6',2"-terpyridine; bpy = 2,2'-bipyridine; Q = quinoline, and CQ = chloroquinoline, chloroquine). The photochemical properties of ligand dissociation for each of these compounds were investigated and compared; additionally, their photoproducts were identified using NMR photolysis. The complexes possess low quantum yields of ligand exchange, but more importantly these complexes were proven not to be dark stable in water, rendering them impractical for PCT. The ability to create a compound capable of efficiently undergoing ligand dissociation when irradiated with low energy light, while it remains stable in the dark would, present a less invasive, controlled method to treat CL with the added potential of eradicating the side effects associated with typical oral treatments. If successful, these techniques can be used in other applications including serving as a noninvasive alternate to current cancer treatments.

Dedication

This thesis is dedicated to my parents, Michael and Pilar Evans.

Acknowledgments

I would like to thank my advisor and mentor Prof. Claudia Turro for her guidance and support in my research and the completing of this thesis. I also wish to acknowledge my fellow group members for providing further direction in the laboratory and via group discussions. A special thanks to TJ Rohrbaugh and Lauren Loftus for sharing their knowledge of ruthenium based syntheses, and Dr. Tanya Whitmer for her instruction on NMR instrumentation techniques.

Vita

- June 2011International Baccalaureate Diploma
Program, York High School
- May 2015B.S. Chemistry, The College of William and
Mary
- 2015-2016Graduate Enrichment Fellow, The Ohio
State University
- 2016-2017Graduate Teaching Associate, Department
of Chemistry, The Ohio State University
- 2017 to present.....GAANN Fellow, The Ohio State
University

Publications

Pike, Robert D.; Ayala, Gerardo; Evans, Alba P. *Journal of Chemical Crystallography*.
2014, *44* (10), 520–526.

Fields of Study

Major Field: Chemistry

Table of Contents

Abstract.....	ii
Dedication.....	iv
Acknowledgments.....	v
Vita.....	vi
List of Tables	ix
List of Figures	x
Chapter 1: Introduction.....	1
Chapter 2: Background	7
2.1 Ruthenium based PDT	7
2.2 Neglected Tropical Diseases – Leishmaniasis	12
Chapter 3: Experimental Methods and Materials	17
3.1 Materials.....	17
3.2 Synthesis and Characterization	18
3.2.1 Synthesis of $[\text{Ru}(\text{tpy})\text{Cl}_3]^0$	18
3.2.2 Synthesis of $[\text{Ru}(\text{tpy})(\text{bpy})\text{Cl}][\text{PF}_6]$	19
3.2.3 Synthesis of $[\text{Ru}(\text{tpy})(\text{bpy})(\text{Q})][\text{PF}_6]_2$	22

3.2.4 Synthesis of Chloroquinoline Base.....	31
3.2.5 Synthesis of [Ru(tpy)(bpy)(CQ)][PF ₆] ₂	32
3.3 Instrumentation.....	41
3.4 Photochemical Methods	42
3.4.1 Extinction Coefficients.....	42
3.4.2 UV-Vis Photolysis	42
3.4.3 Quantum Yields.....	43
3.4.4 NMR Photolysis	45
Chapter 4: Results and Discussion.....	46
4.1 Electronic Absorption	46
4.2 Photolysis in Acetonitrile	49
4.3 Ligand Dissociation via Photoaquation.....	58
Chapter 5: Conclusion.....	62
References.....	64

List of Tables

Table 3.1 ^1H and ^{13}C chemical shifts and multiplicity of $[\text{Ru}(\text{tpy})(\text{bpy})(\text{Q})]^{2+}$ from HSQC (600 MHz, methanol- d_4).	28
Table 3.2 ^1H and ^{13}C chemical shifts and multiplicity of $[\text{Ru}(\text{tpy})(\text{bpy})(\text{CQ})]^{2+}$ from HSQC (600 MHz, methanol- d_4).	38
Table 4.1 Absorption maximum and extinction coefficients of $[\text{Ru}(\text{tpy})(\text{bpy})\text{L}]^{2+}$ compounds in acetone and acetonitrile.	48
Table 4.2 Ligand dissociation quantum yield comparison in CH_3CN at 500 nm.	58

List of Figures

Figure 1.1 Activation of cisplatin (left) through hydrolysis.	1
Figure 1.2 Simplified cisplatin mechanism (a) cellular uptake followed by hydrolysis to the aqua-complex (b) DNA attachment to Guanine N ⁷ (c) cytosine-guanine base pair (d) Pt-DNA intrastrand adduct formed via a crosslink between two adjacent CG pairs (e) kinked DNA followed by apoptosis. ⁸	2
Figure 1.3 Chemical structures of (a) porfimer sodium (Photofrin) (b) 5-ALA-induced Protoporphyrin IX (PpIX) (c) 2-(1-Hexyloxyethyl)-2-devinyl pyropheophorbide-a (Photochlor).	5
Figure 2.1 Photochemical and physical qualities of ground state, spin-allowed and lowest spin-forbidden excited states of [Ru(bpy) ₃] ²⁺ relevant for energy and electron transfer processes (deoxygenated CH ₃ CN, 298 K; the potential values SCE). ^{36,38}	9
Figure 2.2 Simplified Jablonski diagram demonstrating possible excited state transitions for a) ligand dissociation through ³ LF population, b) ¹ O ₂ generation, through ³ ππ* population.	12
Figure 2.3 Chemical structures of anti-protozoal drugs a) chloroquine, b) hydroxychloroquine, and c) amodiaquine.....	15
Figure 3.1 General synthetic scheme for the preparation of complexes of formula [Ru(tpy)(bpy)L][PF ₆] ₂	18

Figure 3.2 Synthetic scheme for $[\text{Ru}(\text{tpy})\text{Cl}_3]^0$	19
Figure 3.3 Synthetic scheme for $[\text{Ru}(\text{tpy})(\text{bpy})\text{Cl}][\text{PF}_6]$	20
Figure 3.4 ^1H NMR (400 MHz, methanol- d_4) and peak assignments for $[\text{Ru}(\text{tpy})(\text{bpy})\text{Cl}][\text{PF}_6]$	21
Figure 3.5 ^1H - ^1H 2D COSY NMR of $[\text{Ru}(\text{tpy})(\text{bpy})(\text{Cl})]^+$ (400 MHz, methanol- d_4).	22
Figure 3.6 Synthetic scheme for $[\text{Ru}(\text{tpy})(\text{bpy})\text{Q}][\text{PF}_6]_2$	23
Figure 3.7 ^1H NMR spectrum (600 MHz, methanol- d_4) and proton assignments for $[\text{Ru}(\text{tpy})(\text{bpy})\text{Q}][\text{PF}_6]_2$	25
Figure 3.8 ^1H - ^1H 2D COSY NMR of $[\text{Ru}(\text{tpy})(\text{bpy})(\text{Q})]^{2+}$ (400 MHz, methanol- d_4).	26
Figure 3.9 ^1H - ^{13}C 2D HSQC NMR of $[\text{Ru}(\text{tpy})(\text{bpy})(\text{Q})]^{2+}$ (600 MHz, methanol- d_4).	27
Figure 3.10 ^1H - ^{13}C 2D HMBC NMR of the ^3J aromatic couplings and ^2J aliphatic couplings of $[\text{Ru}(\text{tpy})(\text{bpy})(\text{Q})]^{2+}$ (600 MHz, methanol- d_4).	29
Figure 3.11 ESI-MS of $[\text{Ru}(\text{tpy})(\text{bpy})\text{Q}]^{2+}$ and $[\text{Ru}(\text{tpy})(\text{bpy})\text{Q}][\text{PF}_6]^+$ in acetonitrile....	30
Figure 3.12 Expanded view of ruthenium isotopic pattern in mass spectrum of compound $[\text{Ru}(\text{tpy})(\text{bpy})\text{Q}]^{2+}$	30
Figure 3.13 ^1H NMR spectrum (400 MHz, methanol- d_4): and proton assignments of Chloroquine base.	32
Figure 3.14 Synthetic scheme for $[\text{Ru}(\text{tpy})(\text{bpy})\text{CQ}][\text{PF}_6]_2$	33
Figure 3.15 ^1H NMR spectrum (600 MHz, methanol- d_4) and proton peak assignments for $[\text{Ru}(\text{tpy})(\text{bpy})\text{CQ}][\text{PF}_6]_2$	35
Figure 3.16 ^1H - ^1H 2D COSY NMR of $[\text{Ru}(\text{tpy})(\text{bpy})(\text{CQ})]^{2+}$ (400 MHz, methanol- d_4). 36	
Figure 3.17 ^1H - ^{13}C 2D HSQC NMR of $[\text{Ru}(\text{tpy})(\text{bpy})(\text{CQ})]^{2+}$ (600 MHz, methanol- d_4). 37	

Figure 3.18 ^1H - ^{13}C 2D HMBC NMR of the ^3J aromatic couplings and ^2J aliphatic couplings of $[\text{Ru}(\text{tpy})(\text{bpy})(\text{CQ})]^{2+}$ (600 MHz, methanol- d_4).	39
Figure 3.19 ESI-MS of $[\text{Ru}(\text{tpy})(\text{bpy})\text{CQ}]^{2+}$ in acetonitrile.	40
Figure 3.20 Expanded view of ruthenium isotopic pattern in mass spectrum of compound $[\text{Ru}(\text{tpy})(\text{bpy})\text{CQ}]^{2+}$	40
Figure 4.1 Electronic absorption spectra of $[\text{Ru}(\text{tpy})(\text{bpy})(\text{CQ})]^{2+}$ (solid line), $[\text{Ru}(\text{tpy})(\text{bpy})(\text{Q})]^{2+}$ (dashed line), and $[\text{Ru}(\text{tpy})(\text{bpy})(\text{py})]^{2+}$ (dotted line) in acetone.....	47
Figure 4.2 Electronic ground state absorption in different solvents for $[\text{Ru}(\text{tpy})(\text{bpy})(\text{Q})]^{2+}$ (solid red line) and $[\text{Ru}(\text{tpy})(\text{bpy})(\text{CQ})]^{2+}$ (dotted green line) in acetone, and $[\text{Ru}(\text{tpy})(\text{bpy})(\text{Q})]^{2+}$ (small dashed blue line), $[\text{Ru}(\text{tpy})(\text{bpy})(\text{CQ})]^{2+}$ (large dashed yellow line) in acetonitrile.	49
Figure 4.3 Photoproduct scheme, solvent substitution of quinoline ligand in acetonitrile upon irradiation.	50
Figure 4.4 Changes to the electronic absorption spectrum of $[\text{Ru}(\text{tpy})(\text{bpy})(\text{Q})]^{2+}$ as a function of time when kept in the dark (top) and following irradiation with >395 nm light (bottom) in CH_3CN	51
Figure 4.5 NMR Photolysis of $69 \mu\text{M}$ $[\text{Ru}(\text{tpy})(\text{bpy})(\text{Q})]^{2+}$ in CH_3CN using royal blue LUXEON Rebel LEDs as the light source ($\lambda_{\text{irr}} \geq 447 \pm 10$ nm).	52
Figure 4.6 Photoproduct scheme, solvent substitution of chloroquinoline ligand in acetonitrile.....	53

Figure 4.7 Changes to the electronic absorption spectrum of $[\text{Ru}(\text{tpy})(\text{bpy})(\text{CQ})]^{2+}$ as a function of time when kept in the dark (top) and following irradiation with >395 nm light (bottom) in CH_3CN .	55
Figure 4.8 NMR Photolysis of $44 \mu\text{M}$ $[\text{Ru}(\text{tpy})(\text{bpy})(\text{CQ})]^{2+}$ in CH_3CN using royal blue LUXEON Rebel LEDs as the light source ($\lambda_{\text{irr}} \geq 447 \pm 10$ nm).	56
Figure 4.9 Changes to the electronic absorption spectrum of $[\text{Ru}(\text{tpy})(\text{bpy})(\text{Q})]^{2+}$ as a function of time when kept in the dark (top: 0, 1, 4, 24 hrs) and following irradiation with >395 nm light (bottom: 0 hr, 20 min, 40 min, 1 hr, 2 hrs, 3 hrs, 4 hrs, 5 hrs, 6 hrs, 7 hrs, 8 hrs, 9 hrs, 10 hrs, 11 hrs, 12 hrs) in water.	60
Figure 4.10 Changes to the electronic absorption spectrum of $[\text{Ru}(\text{tpy})(\text{bpy})(\text{CQ})]^{2+}$ as a function of time when kept in the dark (top: 0 hrs, 2 hrs, 3 hrs, 6 hrs, 24 hrs) and following irradiation with >395 nm light (bottom: 0 mins, 1 min, 5 mins, 10 mins, 20 mins, 40 mins, 60 mins, 120 mins, 6 hrs) in water.	61

Chapter 1: Introduction

Cancer, the second leading cause of death globally after heart disease, is responsible for over half a million deaths annually in the United States alone, and 8.8 million deaths worldwide in 2015.¹ Since the discovery of its ability to inhibit cell division in 1965 by Rosenberg, cisplatin has been at the center of modern day chemotherapy treatments for a variety of cancers, including ovarian, bladder, breast, lung, testicular, gastric, cervical, head and neck tumors and malignant mesothelioma.²

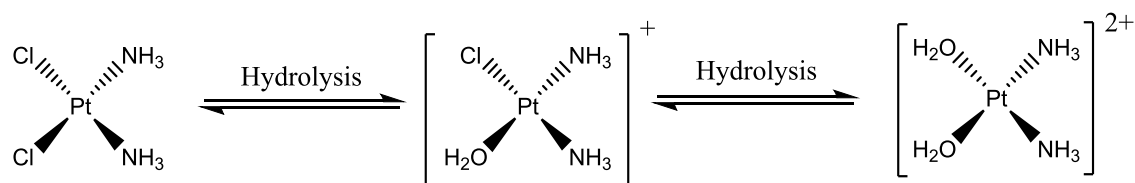


Figure 1.1 Activation of cisplatin (left) through hydrolysis.

When administered into the cell, the square planar platinum complex undergoes aquation due to lower intracellular chloride concentrations compared to the extracellular fluid, thus displacing one of the two chloride ligands with water to give the favored cis- $[\text{PtCl}(\text{NH}_3)_2(\text{H}_2\text{O})]^+$ aqua complex (Figure 1.1).^{3,4} The aqua complex then binds to the N7 of a guanine base on DNA by displacing the recently acquired aqua ligand. This process is typically followed by a subsequent displacement of the second chloride ligand and the compound binds to a second adjacent DNA base, usually another guanine N7 site, as

illustrated in Figure 1.2. This dual displacement and binding is called crosslinking, which causes the double helix to bend at an angle of 78° , thus interfering with mitosis.³ Crosslinking between two adjacent guanines on the same DNA strand, 1,2-intrastrand d(GpG), accounts for 90% of the adducts; although, less common 1,2-intrastrand d(ApG) adducts and 1,3-intrastrand d(GpXpG) adducts can also occur.³⁻⁶ The cell then prompts nucleotide excision repair. Upon recognition that the alteration to the DNA structure is irreparable the cell undergoes apoptosis, a form of programmed self-induced cellular death.^{4,5,7}

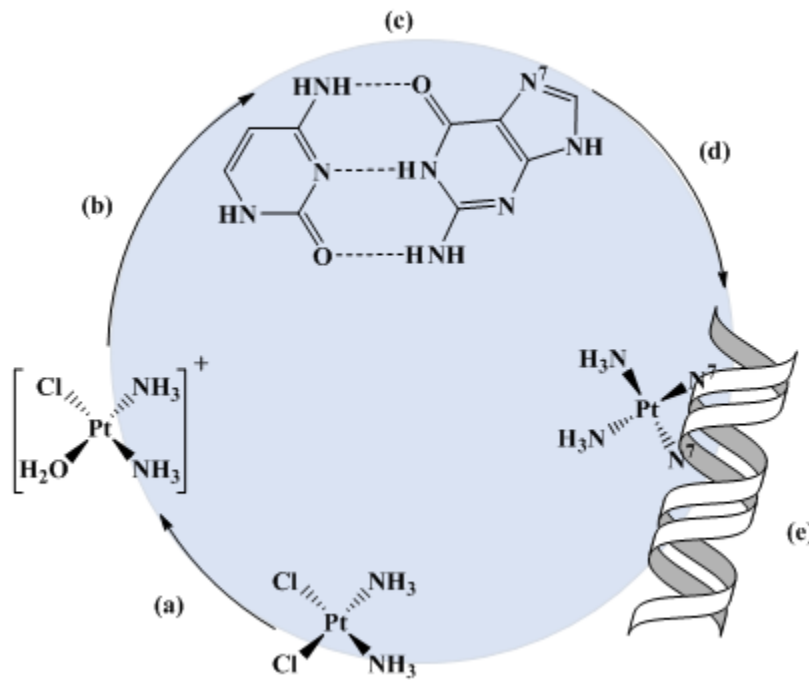


Figure 1.2 Simplified cisplatin mechanism (a) cellular uptake followed by hydrolysis to the aqua-complex (b) DNA attachment to Guanine N^7 (c) cytosine-guanine base pair (d) Pt-DNA intrastrand adduct formed via a crosslink between two adjacent CG pairs (e) kinked DNA followed by apoptosis.⁸

Although cisplatin has proven to be one of the most effective inorganic anticancer agents, significant challenges remain with regards to its mechanism for treating cancer. The most troublesome drawback to intravenous cisplatin treatments is that infected and healthy cells alike undergo apoptosis; thus, healthy tissues and organs are damaged over time.^{7,9} Also, because of drug resistance and considerable side effects including: nausea, neurotoxicity, vomiting, nephrotoxicity, ototoxicity, nausea and anorexia that compromise quality of life, treatment adherence and dosage have to be limited in order to manage them.^{9,10} Despite some promising results in preventing or reducing cisplatin-induced toxicity, there isn't sufficient data to recommend one approach over another in preventing the listed side effects.¹⁰ However, the success of cisplatin and other platinum anticancer derivative drugs has stimulated a renaissance of inorganic medicinal chemistry including the use of photo dynamic therapy (PDT) drugs.¹¹

PDT consists of a photosensitizing agent used to treat malignant tumors upon light activation in an oxygen-rich environment.¹² When used properly, PDT has not shown long-term side effects, is less invasive than surgery with little or no scarring after the irradiated site heals, and is often conducted as an outpatient procedure.¹³ More importantly, it can be used to target specific affected areas very precisely, unlike radiation, PDT can be repeated many times at the same site if needed, and often costs less than other cancer treatments. However, PDT drugs have their limits too, they can only treat areas on or just under the skin, or in the lining of organs that can be reached with a light source.¹²⁻¹⁴ Currently PDT cannot be used to treat cancers that have spread to multiple areas, large cancers, or cancers that have grown deeply into the skin or other organs due to light's inability to travel very

far through body tissues. The most obvious drawback is that special precautions must be taken after the drugs are administered, because treatment leaves patients sensitive to light for some time. PDT treatments are effective with few long-term problems, and thus it is becoming more common place to be used to treat cancer today; however, there are still a lot of limitations that restrict its uses.^{8,12}

Porfimer sodium (Photofrin) and 5-ALA-induced Protoporphyrin IX (PpIX) are among a few FDA approved anticancer photosensitizers currently used in PDT.^{12,15,16} PpIX is used to treat a pre-cancerous skin condition called actinic keratosis (AK). Aminolevulinic acid (ALA) is administered directly onto the affected skin and, rather than laser light, a blue light is used to activate it. Furthermore, methyl ester of ALA, a derivative of ALA, was developed to better facilitate the uptake of PpIX into the afflicted cells and is activated with a red light, unlike its predecessor.^{14,16} However, even with this improvement, PpIX is still somewhat limited to superficial lesions.¹² The ability of the photosensitizer to be activated using low energy red light is of great importance, due to red light's ability to penetrate deeper through skin tissue compared to higher energy light.¹⁷ Accordingly, Photofrin, the most widely used FDA approved PDT in the United States, is activated using a red laser and aids in the treatment of esophageal cancers that otherwise cannot be removed using surgery alone (Figure 1.3). It has also been used to shrink endobronchial tumors, a particular lung cancer that affects the lining of the bronchi.¹⁸ A handful of other new generation photosensitizers are currently undergoing clinical trials. Photochlor, a promising drug, is currently being investigated for its ability to reduce and eradicate esophageal cancer, Barrett's esophagus, basal cell carcinomas, and early and late stages of

lung cancer. Additionally it has a stronger absorbance at shorter wavelengths compared to its predecessors PpIX and Photofrin.^{12,15}

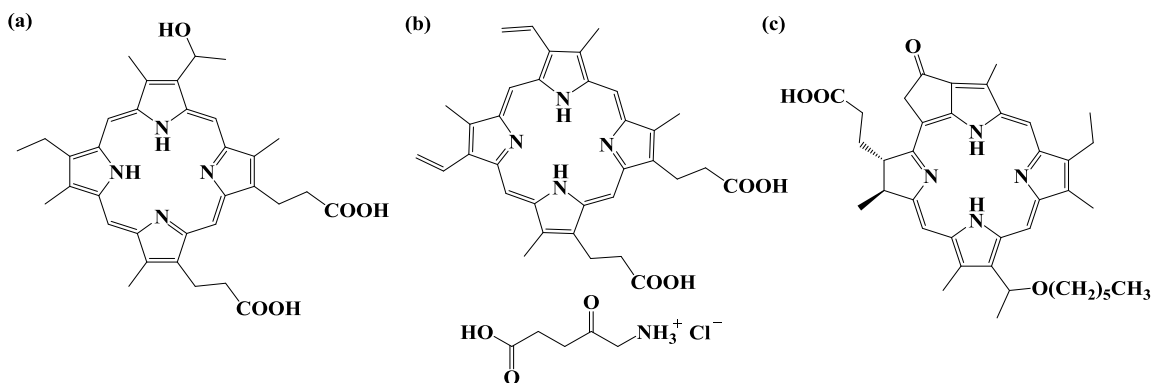


Figure 1.3 Chemical structures of (a) porfimer sodium (Photofrin) (b) 5-ALA-induced Protoporphyrin IX (PpIX) (c) 2-(1-Hexyloxyethyl)-2-devinyl pyropheophorbide-a (Photochlor).

Although phototherapy for the treatment of cancers is relatively new and still undergoing development, the use of light in medicine is not a novel one. The origins of light therapy for medicinal purposes dates as far back as the Greeks and Egyptians.¹⁹ Since then, it has been used to treat patients with mood and sleep disorders including seasonal affective disorder (SAD), a recurrent major depressive illness occurring during the same season each year caused by melatonin suppression.²⁰ Generally, red light helps to encourage collagen production and healing in the skin. It helps to increase blood and oxygen flow to the skin and capillaries, therefore increasing cellular metabolism and strengthening the capillary walls.²¹ Additionally, blue LEDs have proven very effective against more severe acne cases.²² It has been used with the treatment of scars and skin

disorders, including acne vulgaris, eczema, psoriasis, neonatal jaundice, and multiple others.^{19,21-23} Preliminary studies have also shown light therapy is an effective treatment for retinopathy,²⁴ and macular oedema,²⁵ two retinal conditions that affects patients with diabetes. And the list of uses and benefits of phototherapy continues to expand as researchers seek to apply it to treat modern day diseases including Leishmaniasis, Alzheimer's, and Parkinson's.^{26,27}

Chapter 2: Background

2.1 Ruthenium based PDT

Ruthenium polypyridyl complexes have been significant contributors to chemical advances in the fields of solar energy conversion,^{28,29} molecular sensors and switches,³⁰ the understanding of charge transfer reactions,³¹ and photochemotherapy.³²⁻³⁵ Ru(II) polypyridyl complexes are commonly chosen for their unique combination of strong absorption throughout the ultraviolet and visible light regions, chemical stability in solution, long excited state lifetimes, varying substitution rates, demonstrated low toxicity, and suitable redox potentials for biological interactions.^{11,28,35,36} Because of these favorable qualities, ruthenium based complexes have sparked considerable interest in the development of new metallopharmaceutical PDT agents to combat a variety of diseases.

The highly symmetrical compound tris(2,2'-bipyridine)ruthenium(II), $[\text{Ru}(\text{bpy})_3]^{2+}$, a prototypical complex of ruthenium based photochemistry, has been extensively studied for its unique and desirable photochemical characteristics. Thus, it is the standard model complex used as a point of comparison by researchers in comprehending transition metal photochemistry.^{36,37} The Ru(II) hexacoordinate metal center consists of a low spin orbital splitting of the d^6 electron configuration, resulting in completely filling the three lower lying t_{2g} orbitals, while the two higher e_g orbitals remain empty. The complex possesses D_3 symmetry and a preferred octahedral coordination of

ruthenium in both the +2 and +3 oxidation states. It also possesses remarkable thermal and chemical stability in various solvents for extended periods of time, is energetically stable, and kinetically inert to substitution while demonstrating significant backbonding between Ru(II) and the π^* orbitals of bpy.^{36,38} The absorption spectrum of $[\text{Ru}(\text{bpy})_3]^{2+}$ in CH_3CN consists primarily of two ligand-centered (LC) $\pi \rightarrow \pi^*$ transitions in the UV region at 185 and 285 nm, a $d \rightarrow \pi^*$ metal-to-ligand charge transfer (MLCT) in the visible range at 450 nm. In the same solvent the species emits around 600 nm. The lowest energy absorption in the visible spectrum at 450 nm has been assigned to the lowest $^3\text{MLCT}$ excited state of $[\text{Ru}(\text{bpy})_3]^{2+}$. Due to high intersystem crossing rates from the initially populated spin-allowed excited states ($^1\text{MLCT}$), the complex's conversion ($\phi_{^3\text{MLCT}}$) to the lower lying triplet has unit quantum efficiency.³⁶ The $^3\text{MLCT}$ excited state is long-lived, given that the transition back down to the ground state is spin-forbidden. Figure 2.1, from a recent journal review on light driven Ru(II) polypyridyl complexes, summarizes some photophysical and electrochemical properties of $[\text{Ru}(\text{bpy})_3]^{2+}$ upon excitation, reduction, and oxidation. It has long been known that at room temperature in solution $[\text{Ru}(\text{bpy})_3]^{2+}$ can undergo either a ligand centered (LC) reduction process and a metal centered (MC) oxidation process, making its triplet excited state both a good oxidant and reductant.³⁸

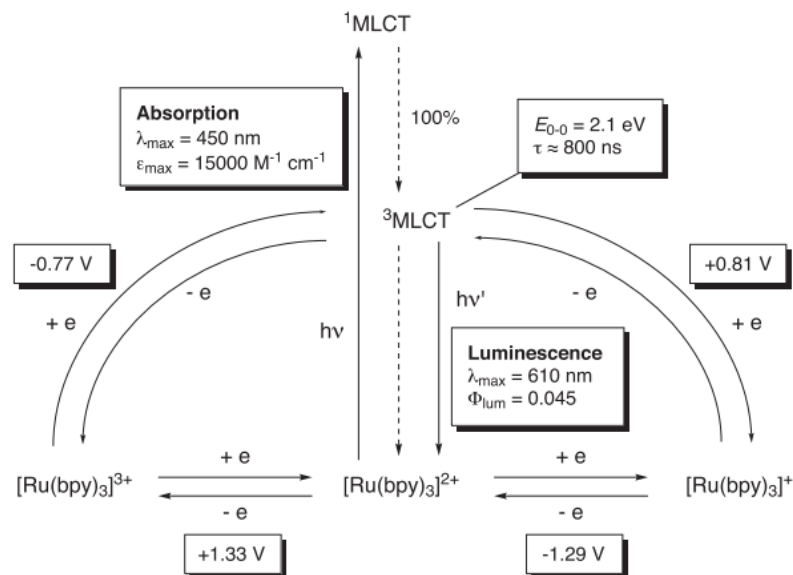


Figure 2.1 Photochemical and physical qualities of ground state, spin-allowed and lowest spin-forbidden excited states of $[\text{Ru}(\text{bpy})_3]^{2+}$ relevant for energy and electron transfer processes (deoxygenated CH_3CN , 298 K; the potential values SCE).^{36,38}

Using $[\text{Ru}(\text{bpy})_3]^{2+}$ as a benchmark, researchers have developed and studied multiple series of ruthenium compounds and how they may be applied to design more efficient PDT agents. Meaningful strides have been made attempting to create potential PDT drugs that absorb efficiently at lower energy wavelengths, have high dark stability in solution, and demonstrate efficient high cytotoxicity when irradiated while remaining nontoxic in the dark. Three modes of action surrounding Ru(II) compounds that can lead to cell death include: biological binding to DNA and proteins, singlet oxygen production, and via ligand dissociation. There are a multitude of investigations underway exploring Ru(II) and Ru(III) coordination complexes and their interactions with nucleic DNA and proteins.³⁹ Namely the recent studies on Ru(II) arene, or piano-stool, complexes have demonstrated the ability to covalently bind to DNA, and with appropriate additional

ligands, may also intercalate between Watson-Crick base pairs.^{40–42} Meanwhile, a variety of other Ru(II) polypyridyl complexes are known to bind to DNA via intercalation, electrostatic binding, or major and minor groove binding.⁴³ These biological interactions cause enough of a structural disturbance to the DNA or protein in question that metabolic cellular mechanisms are unable to repair the damage, and as a result induce cellular death.^{39–41,43}

Another manner in which to achieve cell death, is through the generation of singlet oxygen, or other reactive oxygen species (ROS). Singlet oxygen ($^1\text{O}_2$) is a high-energy form of oxygen that can be used to oxidize proteins or lipids which often can cause cell death via apoptosis or, the less desired, painful, necrosis. A variety of photosensitizers with π -extended systems, including diimine (1,10-phenanthroline derivatives) and cyclometalated (2-phenylpyridine derivatives) ligands, have been used to generate singlet oxygen in attempts to promote apoptosis in bacterial and cancer cells alike.^{32,43,44} The nature of π -extended systems introduces long-lived, low-lying, accessible $^3\pi\pi^*$ ligand centered excited states, that in turn, upon their population, generate $^1\text{O}_2$.⁴⁵ The singlet oxygen quantum yield (ϕ_Δ) is a quantitative measurement of the efficiency in which photosensitizers are able to use energy, in the form of light, to convert oxygen in the ground state to the reactive species $^1\text{O}_2$ useful in photodynamic therapy. The ϕ_Δ is typically described as the number of molecules of singlet oxygen generated per number of photons absorbed by the sensitizer, and is used to quantify the efficiency of $^1\text{O}_2$ generation. Some of the most efficient $^1\text{O}_2$ producing ligands include benzo[i]dipyrido[3,2-a:2',3'-c]phenazine (dppn) and 3-(pyridin-2-yl)benzo[i]dipyrido[3,2-a:2',3'-c]phenazine (pydppn)

with quantum yields of near complete efficiency.³²⁻³⁴ The major drawback to this method of photocytotoxicity is the dependence on an oxygen source that may not be available in hypoxic environments that breed cancer.^{15,46}

An alternative approach to achieving cytotoxicity consists of using a metal-centered complex, with little to no biological influence on its own, and binding a current organic drug compound of known therapeutic value to create a dark-stable inactive drug system. The metal scaffold acts as a carrier and stabilizer for the drug, while the organic drug protects the metal from interacting in potential competing biological side reactions before the pair reaches its desired target location where both can then be activated using the desired wavelength of light.¹¹ Thus another cytotoxic method, and the focus of this study, consists of a caged drug made available via selective small molecule release, or ligand dissociation. There are multiple studies demonstrating successful dissociation and exchange of pyridyl based ligands, which in some cases are made possible due to the addition of steric bulk they impose on the pseudo-octahedral molecule.^{32-35,47} This added strain causes further distortion of the pseudo-octahedral geometry around the metal center, lowering the metal centered 3LF state, and thus making it easier to electronically populate. Initially, a photon, via irradiation, excites the complex from the Ru(II) ground state to the 1MLCT excited state; then, via intersystem crossing, it proceeds to populate the 3MLCT , the lowest energy excited state for most Ru(II) polypyridine complexes. If the 3LF state is comparatively low enough in energy, the complex undergoes internal conversion, populating this σ antibonding state causing the desired ligand dissociation.³⁶ Figure 2.2 briefly summarizes this dissociative process. It has been determined that the efficiency of

dissociation is not extensively based on the strength of the metal-ligand bond, as the Ru-L bond strength is indicative of the complex in its ground state configuration.³⁵ Therefore, the efficiency of ligand dissociation is primarily dependent upon the ability to populate a low lying ^3LF state. Recently this concept has been successfully applied towards the treatment of Chagas disease, a highly prevalent ailment in Latin America. The administration of imidazole-base fungicides, clotrimazole and ketoconazole, via ligand photo-release proved highly efficient against *Trypanosoma cruzi*, the parasite responsible for Chagas disease.^{11,48,49}

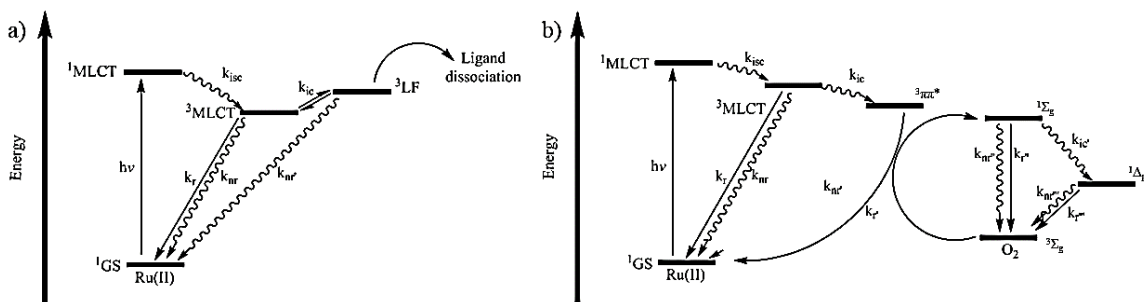


Figure 2.2 Simplified Jablonski diagram demonstrating possible excited state transitions for a) ligand dissociation through ^3LF population, b) $^1\text{O}_2$ generation, through $^3\pi\pi^*$ population.

2.2 Neglected Tropical Diseases – Leishmaniasis

Neglected tropical diseases (NTDs) are a group of 17 illnesses that prevail in 149 countries across the globe and affect more than one billion individuals, costing developing economies billions of dollars annually and claiming 534,000 lives annually worldwide.^{50–}

⁵² Although the number of diseases on the list have decreased with infections like malaria

and tuberculosis receiving more global attention in the last couple decades, parasitic ailments Chagas disease, leprosy, and Leishmaniasis are still prevalent in impoverished geographical areas.^{26,48,52} Leishmaniasis, caused by intracellular hemoflagellate protozoan parasites, is a potentially fatal inflammatory NTD found in over 98 countries located in Asia, Africa, the Americas, and southern Europe with approximately 20 *Leishmania* species that cause the most common form, cutaneous Leishmaniasis (CL).²⁶ CL is transmitted through the bite of an infected female *phlebotomine* sand fly, which then manifests itself in the form of skin ulcers and severe rashes. In some cases, CL can progress to visceral (VL) and mucosal *Leishmania* (ML), both of which have high fatality rates and current treatments for these are often extreme and highly invasive.⁵²

When a human host is bitten by an infected, female, carrier sand fly, the *Leishmania* parasite is transmitted to the epidermal skin cells surrounding the open bite wound via a combination of the insect's blood and saliva. The parasite then uses mononuclear host cells to replicate and infect adjacent cells, causing skin irritation and the development of open sores. Although the pathogenesis of ML is still unclear it is believed that it is the effect of gradual expansion of CL lesions to the mucosal region that have been left untreated, or as a result of metathesis.⁵³ On the other hand, VL manifests when the parasites are taken up by phagocytic cells, cells designed to remove foreign pathogens and debris, and carried throughout the reticuloendothelial system (the cellular portion of the immune system) to the host's internal organs.⁵⁴ Once there, the parasites cause severe inflammation and disfiguration of the organ tissues via ulcers.

Analogous to Leishmaniasis, malaria is a life-threatening parasitic disease that is also transferred by the bite of an infected female insect (*Anopheles* mosquito). Due to the similarities of the two tropical diseases, current antimalarial drugs prove to be efficient at combatting the various forms of Leishmaniasis.^{48,55} Chloroquine diphosphate (CQDP, or CQ for chloroquine) is an anti-protozoal drug widely used and primarily developed for the prevention and treatment of malaria, but has been effective against other protozoal related illnesses. Once administered the weak base drug is absorbed into the cellular membrane of the parasite via vacuole ingestion. Once inside the food vacuole, more specifically the lysosome, the drug undergoes ionization due to the acidic conditions inside the parasitic lysosome. With an internal acidic pH of 5.5, CQ is most prevalent in its double protonated state, rendering its most ionized form (2+) unable to exit the lysosome.⁵⁶ Over a short period of time, CQ²⁺ builds in concentration inhibiting the polymerization of the hemoglobin breakdown product heme into hemozoin, a non-toxic pigment found in blood, which in turn causes an accumulation of free heme. It is the toxicity caused by the acute buildup of free heme that then kills the *Leishmania* parasites in the same manner it does malarial protozoa.⁵⁷ Recent studies have indicated that this drug may also harbor antitumor properties, due to its ability to accumulate in lysosomes and disrupt the regular cellular process of autophagy.⁵⁸

Similar to many successful pathogens, *Leishmania* has developed strategies to evade host immune mechanisms to survive within the host, thus making them more difficult to eliminate with regular CQ treatments.^{53,58,59} Hydroxychloroquine (HCQ), a chloroquine analog has proven in recent studies to exert a higher level of potency and

cytotoxic effects on drug-sensitive and resistant glioma cells than its CQ parent.⁵⁸ Similarly, amodiaquine (AQ) has proven effective against chloroquine-resistant *P. falciparum* malarial strains, although it is often avoided due to its unlikely yet more severe side effects including damaging the liver and causing seizures, but has been occasionally used as a last resort in well-developed Leishmanial cases (Figure 2.3).^{59,60}

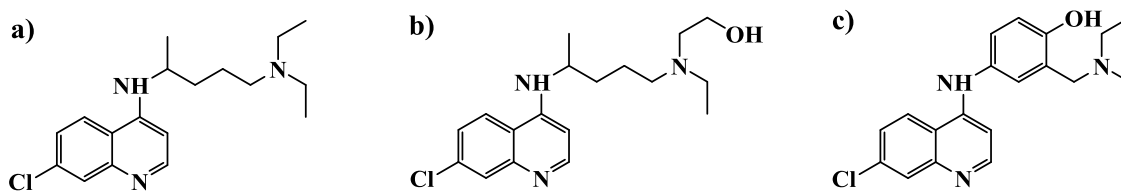


Figure 2.3 Chemical structures of anti-protozoal drugs a) chloroquine, b) hydroxychloroquine, and c) amodiaquine.

In the treatment of CL and malaria, CQ and its derivatives are taken orally in the form of a tablet. Oral medicines often pass through the liver before entering the bloodstream and reaching their intended bodily target, often causing a list of side effects. CQ's side effects include, but are not limited to fatigue, loss of appetite, nausea, and stomach cramps.⁵⁶ Thus, currently available therapeutic methods and drugs are toxic, outdated, and reported to have little efficiency with the current strains; consequently, researchers are turning to new methods of drug delivery.⁵⁰ For a topical disease like CL it would of interest to administer drugs via a method that avoids unnecessary systemic exposure, by delivering it directly in a controlled fashion to the area of interest. Photosensitizers are considered one of the major leaders in the development of new drugs to treat cutaneous diseases due to their comparative low systemic toxicity by targeting drug

activity using a controlled light source, thus presenting a non-invasive mode of therapy. Improved treatment of CL will further prevent the progression to VL and ML lethal forms.¹⁵

Chapter 3: Experimental Methods and Materials

3.1 Materials

All solvents and chemicals were used as received unless otherwise noted. The chemicals chloroquine diphosphate, 2,2'-bipyridine, ruthenium trichloride trihydrate, silver trifluoromethanesulfonate, lithium chloride, triethylamine, sodium acetate trihydrate, alumina oxide (neutral, activated, Brockmann I grade) used for column chromatography, and NMR solvents deuterated acetone, methanol, and acetonitrile were obtained from Sigma-Aldrich. Quinoline and ammonium hexafluorophosphate were purchased from Acros Organics. Ammonium hydroxide solution was obtained from EMD Millipore Sigma, while absolute 200 proof ethanol was obtained from Decon Labs, 1,10-phenanthroline from Fluka Chemical, and chloroquine (base) from Ark Pharm. Potassium tris(oxalate)ferrate(III) trihydrate (also referred to as ferrioxalate) and 2,2',2''-terpyridine were purchased from Strem Chemicals. Celite 545 Filter Aid and the following solvents: methanol, diethyl ether anhydrous, chloroform, sulfuric acid, acetone, toluene, and acetonitrile were all obtained from Fisher Chemical and used as received unless otherwise stated. All water used in reactions and metatheses steps was deionized using a Barnstead Fi-stream filter purification system to 18 M Ω .

3.2 Synthesis and Characterization

In general, the complexes were synthesized starting from $\text{Ru}(\text{tpy})\text{Cl}_3$ which was prepared from $\text{RuCl}_3 \cdot \text{H}_2\text{O}$ following a literature procedure described below. The 2,2'-bipyridyl bidentate ligand was then added to the $[\text{Ru}(\text{tpy})\text{Cl}_3]^0$ scaffold to form $[\text{Ru}(\text{tpy})(\text{bpy})\text{Cl}]^+$, which in turn was used as the primary starting reagent for the $[\text{Ru}(\text{tpy})(\text{bpy})\text{L}]^{2+}$ complexes as outlined generically in Figure 3.1. The synthetic details of the procedures for each complex are described below along with their respective purification steps.

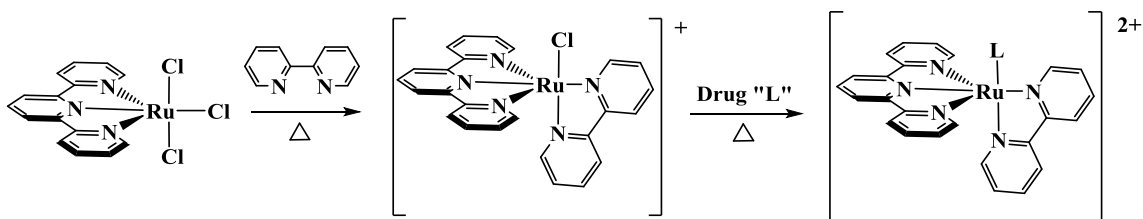


Figure 3.1 General synthetic scheme for the preparation of complexes of formula $[\text{Ru}(\text{tpy})(\text{bpy})\text{L}][\text{PF}_6]_2$.

3.2.1 Synthesis of $[\text{Ru}(\text{tpy})\text{Cl}_3]^0$

$[\text{Ru}(\text{tpy})\text{Cl}_3]^0$ was prepared following a method previously reported.⁶¹ In a 200 mL round bottom flask, equipped with a stir bar, 125 mL of absolute ethanol was purged with nitrogen for 30 minutes. To the deaerated solution, 340.7 mg (1.30 mmol, FW: 261.44 g/mol) of $\text{RuCl}_3 \cdot \text{H}_2\text{O}$ was added, followed by 301.2 mg (1.29 mmol, FW: 233.27 g/mol)

of 2,2',2''-terpyridine. The reaction mixture (Figure 3.2) was heated at reflux for 4 hours, while maintaining vigorous stirring.

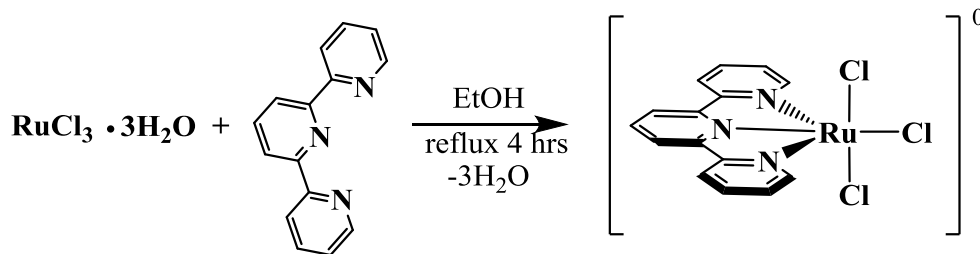


Figure 3.2 Synthetic scheme for $[\text{Ru}(\text{tpy})\text{Cl}_3]^0$.

Once the solution cooled to room temperature, a brown precipitate was filtered from the reddish yellow filtrate, and washed with three 30 mL portions of absolute ethanol to remove $[\text{Ru}(\text{tpy})_2]^{2+}$. The brown powder was then washed with three 30 mL portions of diethyl ether (Et_2O) to remove any excess tpy, and air dried. Yield: 525.1 mg (93%).

3.2.2 Synthesis of $[\text{Ru}(\text{tpy})(\text{bpy})\text{Cl}][\text{PF}_6]$

$[\text{Ru}(\text{tpy})(\text{bpy})\text{Cl}][\text{PF}_6]$ was synthesized following previously reported procedures with a few modifications.^{62,63} A 301.4 mg (0.68 mmol) quantity of $[\text{Ru}(\text{tpy})\text{Cl}_3]^0$, 160.2 mg (1.02 mmol) of 2,2'-bipyridine, and 143.9 mg (3.40 mmol, FW: 42.34 g/mol) of LiCl were added to a 100 mL round bottom equipped with a stir bar. The reactants were dissolved in a 40 mL 3:1 (v/v) ethanol : water, containing 200 μL of triethylamine (Et_3N) as a reductant (Figure 3.3). After heating at reflux for 4 hours, the volume of the solution was reduced to remove ethanol (EtOH) via rotary evaporation. The concentrated pot solution was then

added dropwise to a stirring concentrated NH_4PF_6 aqua slurry and allowed to stir for 1 hour. The dark purple salt precipitated out of solution, was collected, and washed with two 10 mL portions of chilled distilled water followed by 20 mL of anhydrous diethylether (Et_2O).

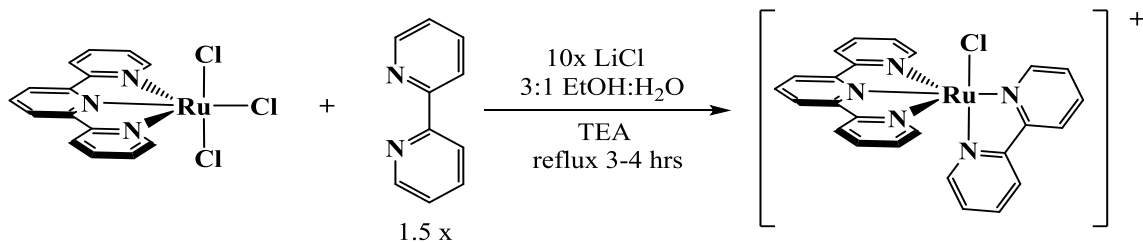


Figure 3.3 Synthetic scheme for $[\text{Ru}(\text{tpy})(\text{bpy})\text{Cl}][\text{PF}_6]$.

The air-dried powder was dissolved in 10 mL of 1:1 (v/v) toluene/acetone and was then filtered and chromatographed on an alumina I (neutral) column using 3:2 (v/v) toluene/acetone as the eluent. Two bands separate, the slower orange band is $[\text{Ru}(\text{tpy})_2][\text{PF}_6]_2$, while the faster eluding purple band was collected, reduced in volume to concentrate (10 mL), and added dropwise to a stirring ether bath to remove residual toluene solvent. The product precipitated as a purple black crystalline powder in ether, was filtered onto a frit, and washed with 20 mL of Et_2O . Yield: 270.1 mg (59%). ^1H NMR (400 MHz, *methanol-d*₄): δ (ppm): 10.20 (d, $J = 5.52$ Hz, 1H), 8.76 (d, $J = 8.12$ Hz, 1H), 8.65 (d, $J = 8.08$ Hz, 2H), 8.53 (d, $J = 8.04$ Hz, 2H), 8.48 (d, $J = 8.12$ Hz, 1H), 8.32 (td, $J = 8.04$, 1.52 Hz, 1H), 8.16 (t, $J = 8.08$ Hz, 1H), 8.00 (td, $J = 7.55$, 1.20 Hz, 1H), 7.94 (td, $J = 7.72$, 1.48

Hz, 2H), 7.74 (td, $J = 7.88, 1.40$ Hz, 1H), 7.70 (d, $J = 4.84$ Hz, 2H), 7.38 (d, $J = 5.77$ Hz, 1H), 7.33 (td, $J = 6.57, 1.24$ Hz, 2H), 7.04 (td, $J = 6.63, 1.32$ Hz, 1H), assignments as shown in Figure 3.4, which is consistent with previous work.⁶⁴ Furthermore, two dimensional homonuclear correlation spectroscopy (COSY), which is used to identify proton-proton spins that are 3J coupled, was used to assign proton peaks (Figure 3.5).

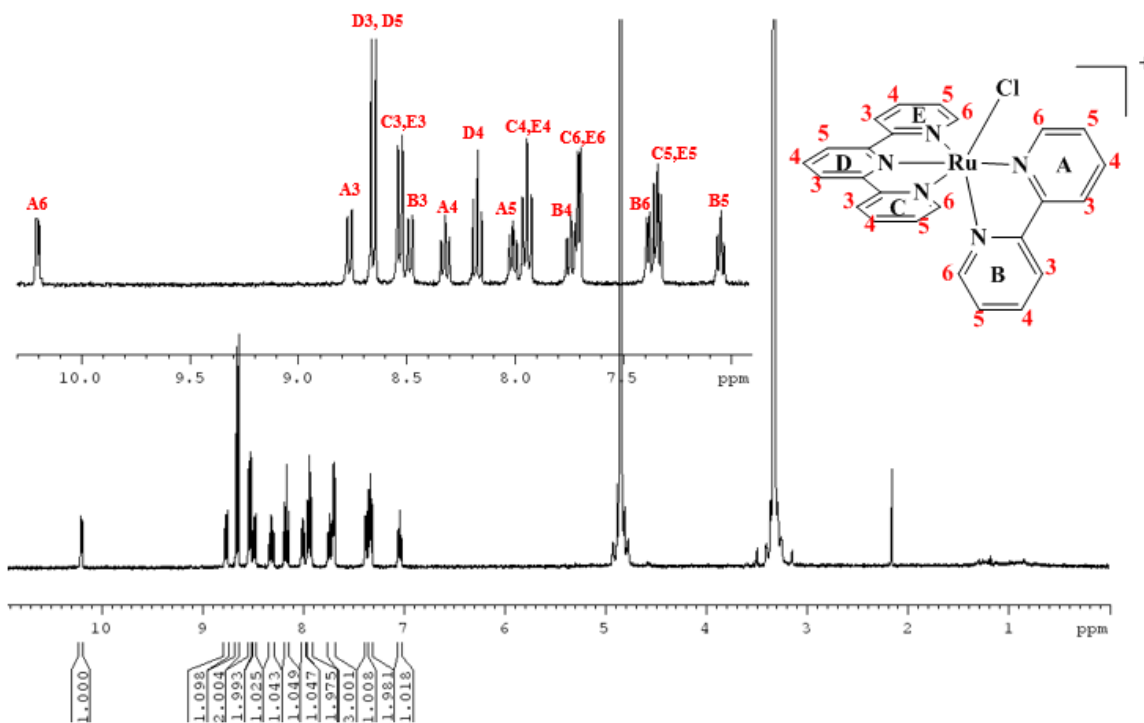


Figure 3.4 ^1H NMR (400 MHz, $\text{methanol-}d_4$) and peak assignments for $[\text{Ru}(\text{tpy})(\text{bpy})\text{Cl}][\text{PF}_6]$.

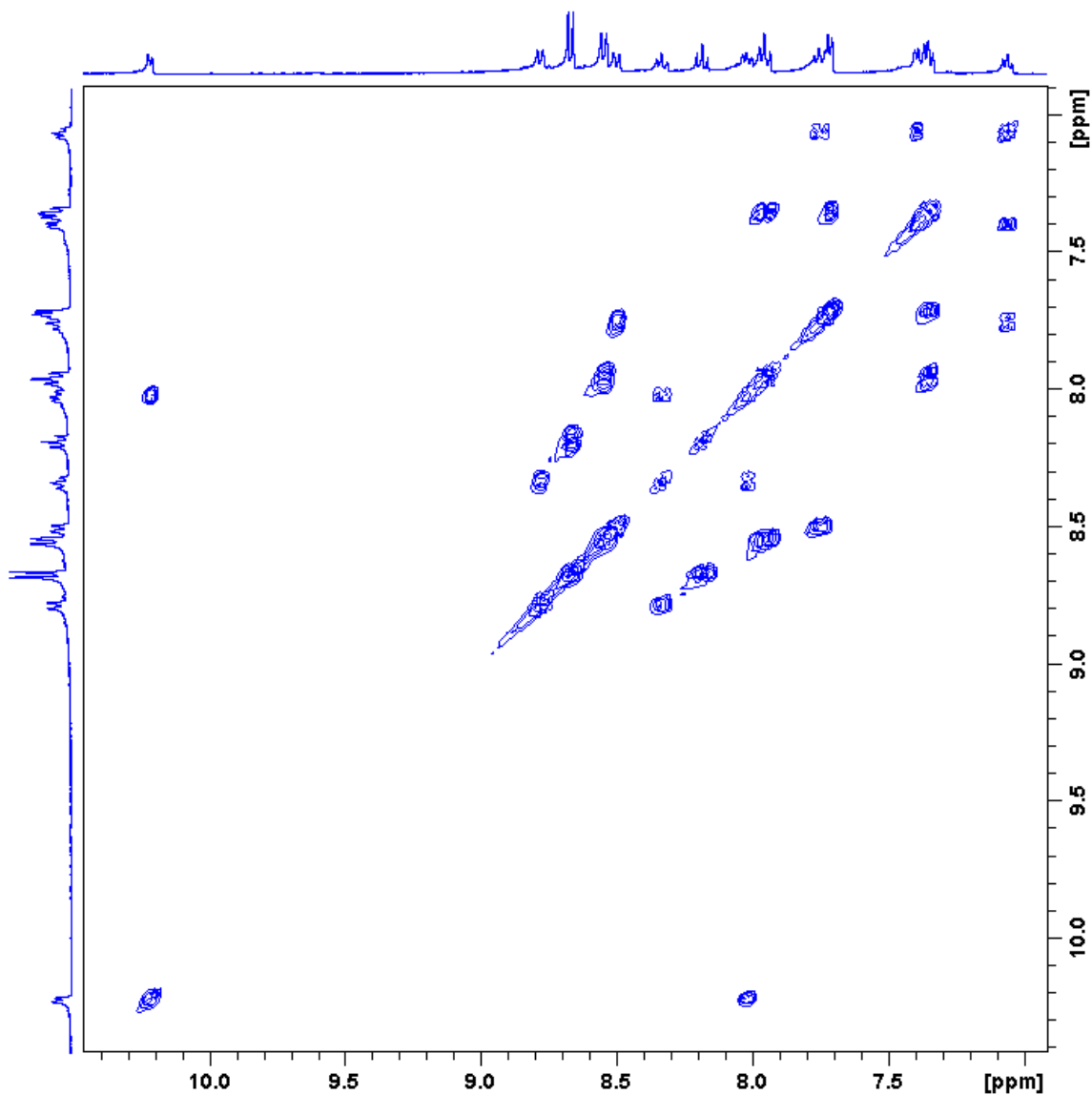


Figure 3.5 ^1H - ^1H 2D COSY NMR of $[\text{Ru}(\text{tpy})(\text{bpy})(\text{Cl})]^+$ (400 MHz, *methanol-d*₄).

3.2.3 Synthesis of $[\text{Ru}(\text{tpy})(\text{bpy})(\text{Q})][\text{PF}_6]_2$

$[\text{Ru}(\text{tpy})(\text{bpy})(\text{Q})][\text{PF}_6]_2$ (Q = quinoline) was prepared using similar steps reported in literature for the binding of similar pyridyl ligands.^{35,65} In a 50 mL round bottom flask, equipped with a stir bar, 21.5 mg (0.03 mmol) of $[\text{Ru}(\text{tpy})(\text{bpy})\text{Cl}][\text{PF}_6]$ was added,

followed by 15.4 mg (0.06 mmol) of silver trifluoromethanesulfonate (AgOTf), and 1 mL (1.09 g, 8.44 mmol) of 99% pure quinoline ligand (Q) (1.09 g/cm³). The contents were heated at reflux in 20 mL of absolute EtOH, previously purged with N₂, covered in foil overnight for at least 16 hours (Figure 3.6). All the following steps were also conducted in a light free or reduced environment.

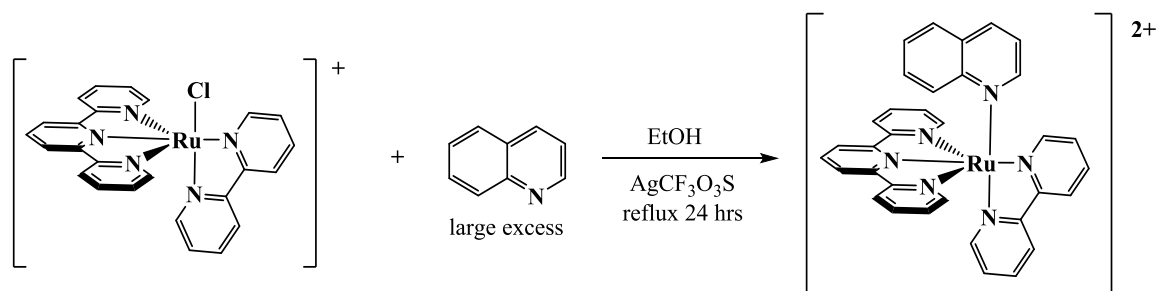


Figure 3.6 Synthetic scheme for [Ru(tpy)(bpy)Q][PF₆]₂.

The room temperature solution was filtered through celite to remove AgCl. The filtrate was then added dropwise to a stirring NH₄PF₆ aqua slurry, filtered, washed with 20 mL of water followed by 20 mL of Et₂O, and suction dried to yield a red-orange precipitate. The powder was then dissolved in 5 mL of 1:1 (v/v) toluene/acetone and chromatographed on an alumina I (neutral) column using 2:3 (v/v) toluene/acetone as the eluent. The slower orange band was collected, rotary evaporated down to dryness, dissolved in acetone and reprecipitated in ether three times before filtering. The light orange powder was air dried. Yield: 13.6 mg (50%). ¹H NMR and residual coupled ¹³C (600 MHz, *methanol-d*₄) δ (ppm): 8.88 (d, J = 8.28 Hz, 1H, ¹³C = 125.92), 8.80 (d, J = 5.52 Hz, 1H, ¹³C = 153.45),

8.71 (d, $J = 8.16$ Hz, 2H, $^{13}\text{C} = 125.19$), 8.63-8.60 (m, 3H, $^{13}\text{C} = 126.35, 125.22$), 8.45 (s, 1H, $^{13}\text{C} = 157.36$), 8.37 (td, $J = 7.84, 1.38$ Hz, 1H, $^{13}\text{C} = 139.31$), 8.25 (t, $J = 8.13$ Hz, 1H, $^{13}\text{C} = 137.74$), 8.12 (td, $J = 7.88, 1.41$ Hz, 2H, $^{13}\text{C} = 140.06$), 7.97 (d, $J = 5.35$ Hz, 2H, $^{13}\text{C} = 154.31$), 7.91-7.88 (m, 3H, $^{13}\text{C} = 138.91, 127.82, 129.08$), 7.82-7.80 (m, 2H, $^{13}\text{C} = 134.47, 129.02$), 7.68-7.65 (m, 3H, $^{13}\text{C} = 124.88, 130.75, 143.98$), 7.54 (td, $J = 6.60, 1.20$ Hz, 2H, $^{13}\text{C} = 130.13$), 7.42 (d, $J = 5.58$ Hz, 1H, $^{13}\text{C} = 152.28$), 7.19 (td, $J = 6.69, 1.26$ Hz, 1H, $^{13}\text{C} = 128.26$), shown in Figure 3.7. NMR assignments and residual carbon shifts were determined using a combination of three different two-dimensional NMR spectroscopic techniques. The COSY NMR is shown in Figure 3.8. Heteronuclear single quantum correlation (HSQC), the resulting spectrum shown in Figure 3.9, was used to determine the residual carbon chemical shifts coupled to the adjacent protons in question listed in Table 3.1. Heteronuclear multiple-bond correlation spectroscopy (HMBC), was used to detect heteronuclear correlations between ^1H and ^{13}C over longer range (Figure 3.10). The instrument probe was calibrated to detect ^3J couplings in the aromatic region for HMBC experiments. ESI MS: m/z 310.06, corresponding to $[\text{Ru}(\text{tpy})(\text{bpy})\text{Q}]^{2+}$ and m/z 765.08, corresponding to $[\text{Ru}(\text{tpy})(\text{bpy})\text{Q}][\text{PF}_6]^+$ shown in Figures 3.11 and 3.12.

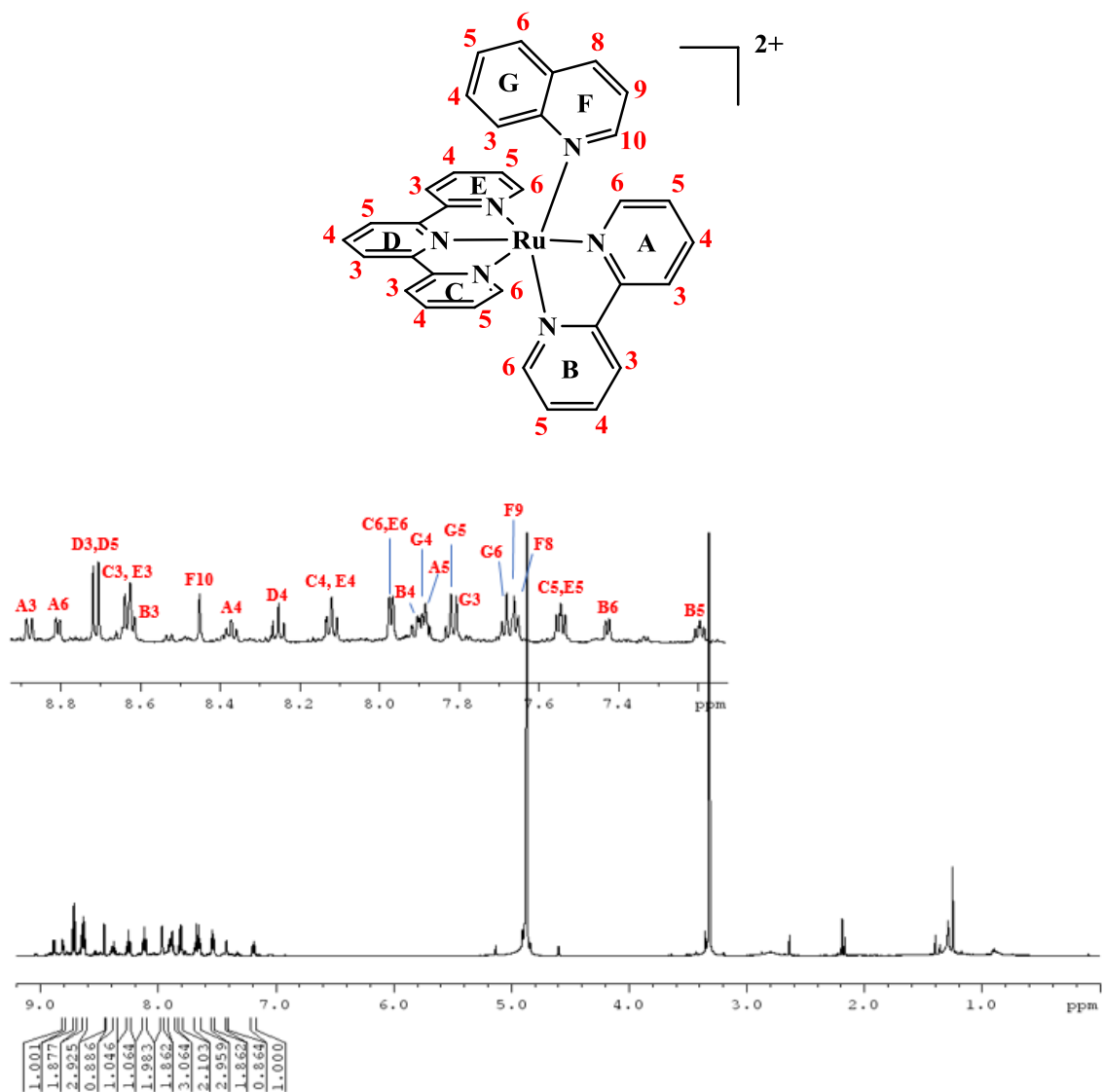


Figure 3.7 ¹H NMR spectrum (600 MHz, *methanol-d*₄) and proton assignments for [Ru(tpy)(bpy)Q][PF₆]₂.

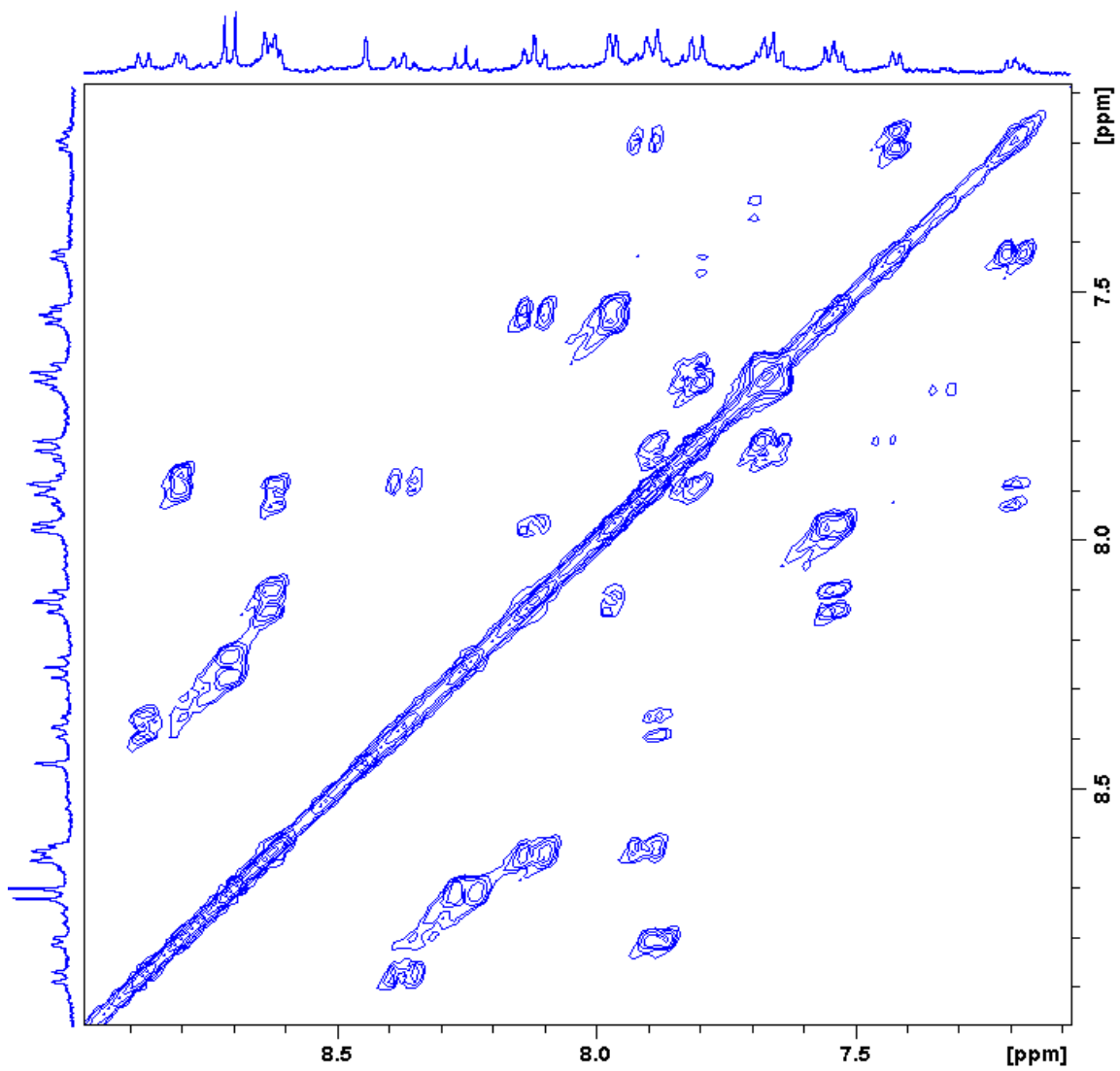


Figure 3.8 ^1H - ^1H 2D COSY NMR of $[\text{Ru}(\text{tpy})(\text{bpy})(\text{Q})]^{2+}$ (400 MHz, *methanol-d*₄).

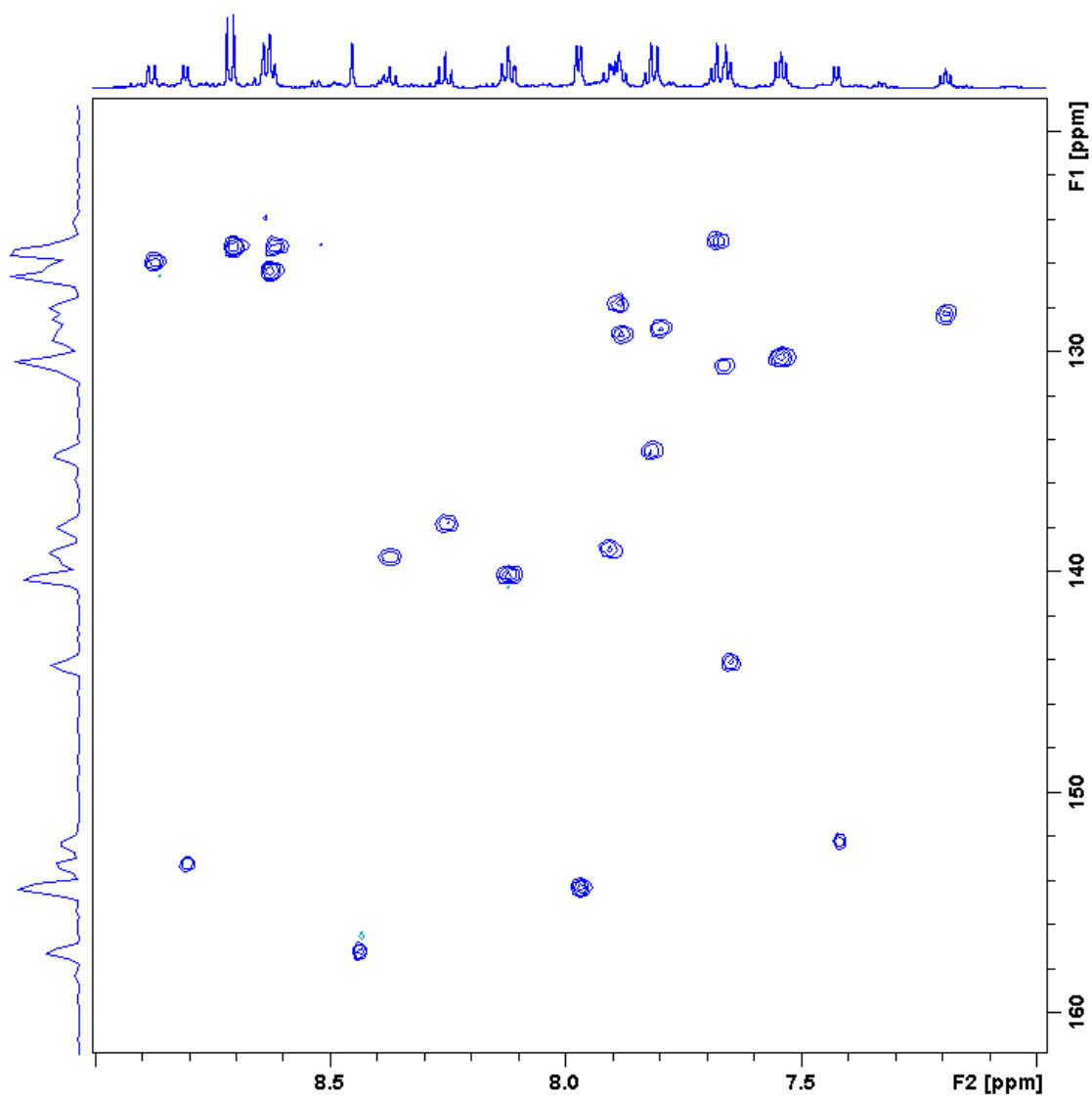


Figure 3.9 ^1H - ^{13}C 2D HSQC NMR of $[\text{Ru}(\text{tpy})(\text{bpy})(\text{Q})]^{2+}$ (600 MHz, *methanol-d*₄).

Table 3.1 ^1H and ^{13}C chemical shifts and multiplicity of $[\text{Ru}(\text{tpy})(\text{bpy})(\text{Q})]^{2+}$ from HSQC (600 MHz, *methanol-d*₄).

Label	Multiplicity	^1H (ppm)	^{13}C (ppm)
A3	d	8.88	125.92
A6	d	8.80	153.45
D3, D5	d	8.71	125.19
C3, E3	m (d)	8.63	126.35
B3	m (t)	8.62	125.22
F10	s	8.45	157.36
A4	td	8.37	139.31
D4	t	8.25	137.74
C4, E4	td	8.12	140.06
C6, E6	d	7.94	154.31
B4	m	7.91	138.91
G4	m (td)	7.89	127.82
A5	m	7.88	129.08
G5	m (t)	7.82	134.47
G3	m (d)	7.80	129.02
G6	m	7.68	124.88
F9	m	7.66	130.75
F8	m	7.65	143.98
C5, E5	td	7.54	130.13
B6	d	7.42	152.28
B5	td	7.19	128.26

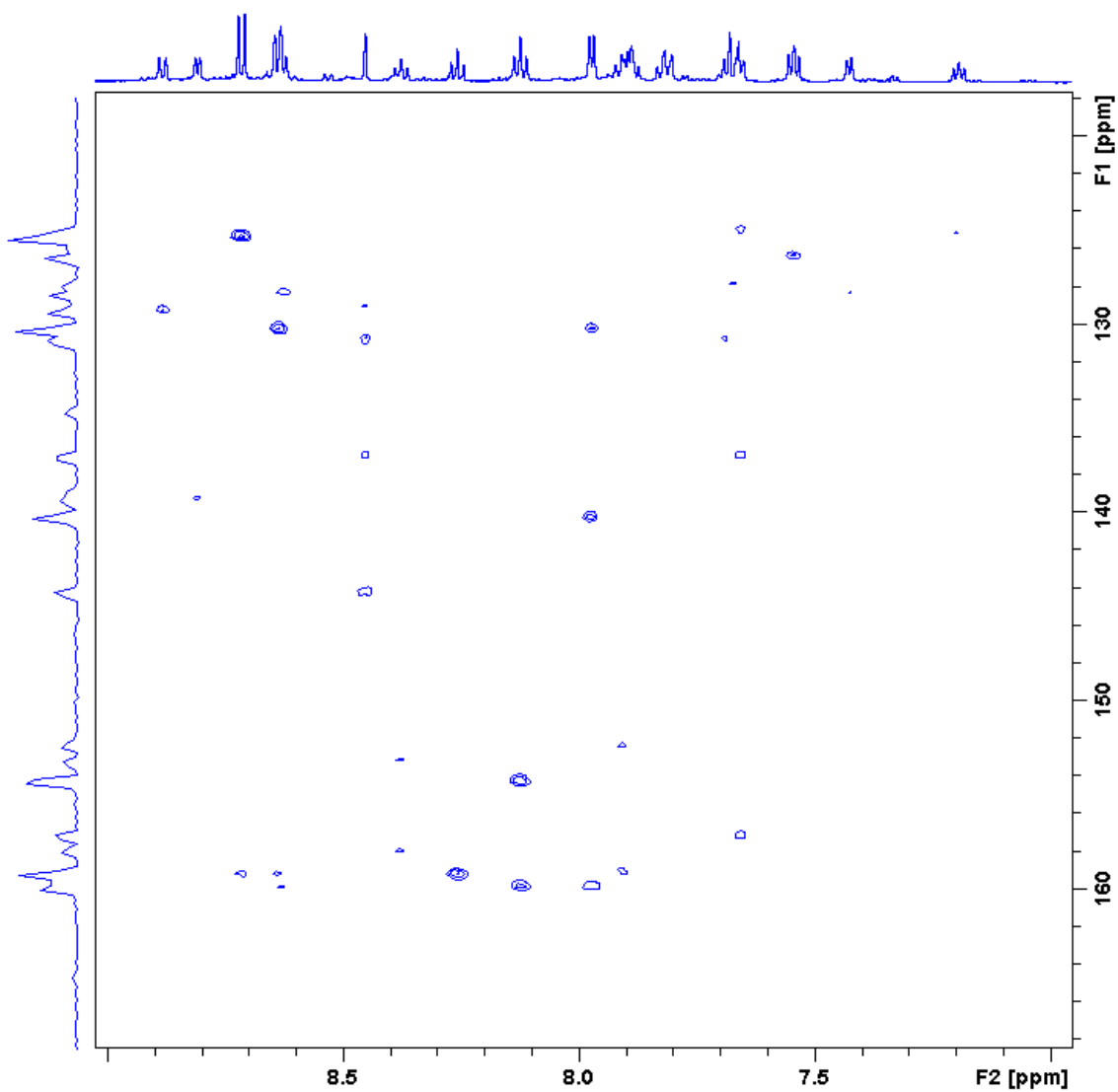


Figure 3.10 ^1H - ^{13}C 2D HMBC NMR of the ^3J aromatic couplings and ^2J aliphatic couplings of $[\text{Ru}(\text{tpy})(\text{bpy})(\text{Q})]^{2+}$ (600 MHz, *methanol-d*₄).

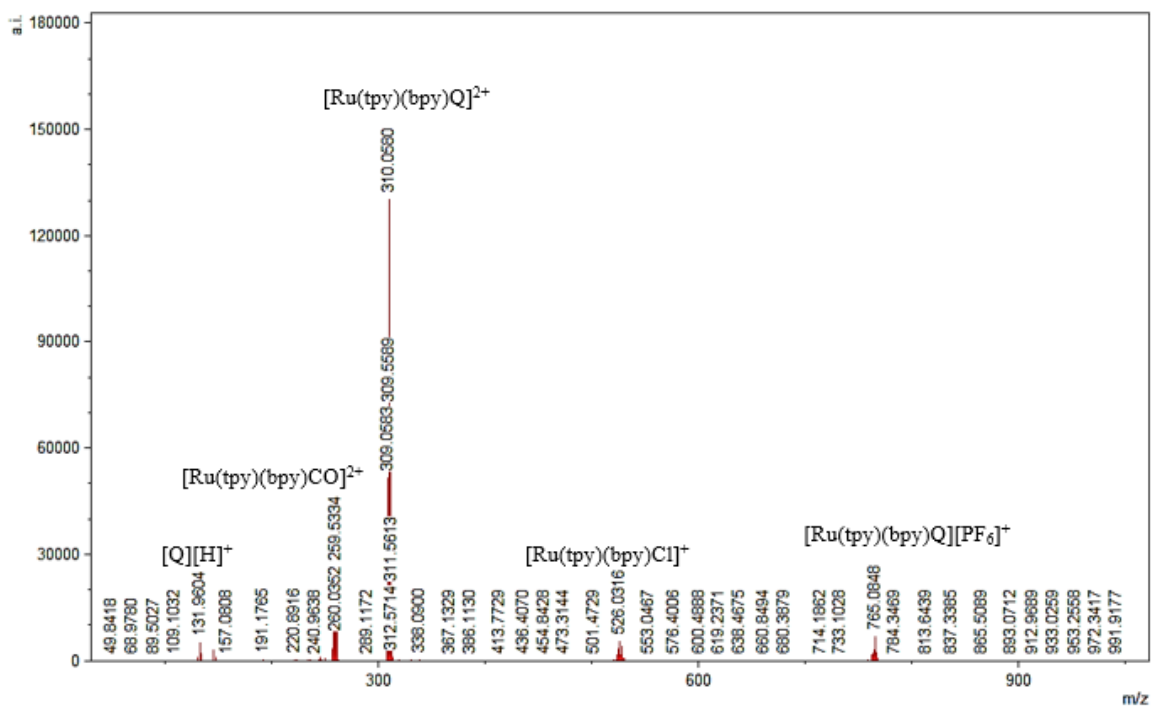


Figure 3.11 ESI-MS of $[\text{Ru}(\text{tpy})(\text{bpy})\text{Q}]^{2+}$ and $[\text{Ru}(\text{tpy})(\text{bpy})\text{Q}][\text{PF}_6]^+$ in acetonitrile.

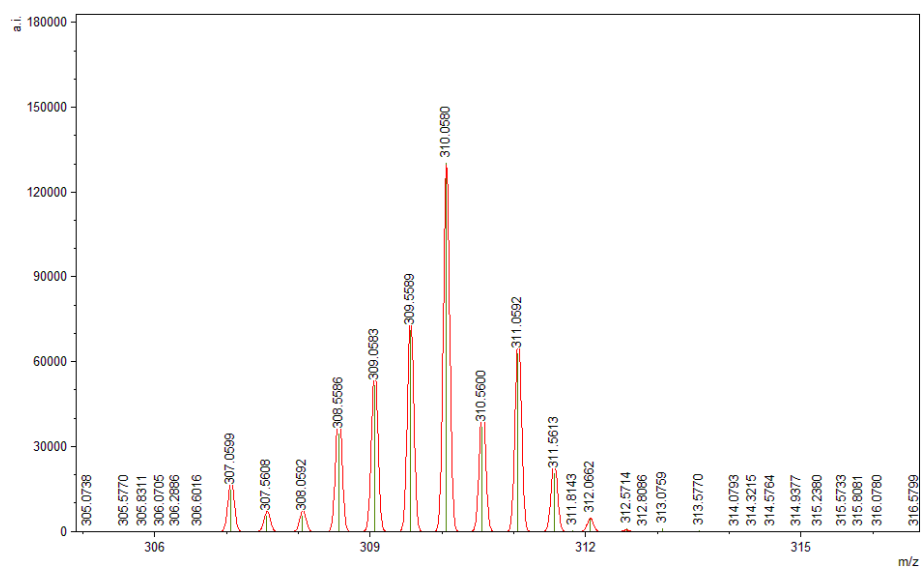


Figure 3.12 Expanded view of ruthenium isotopic pattern in mass spectrum of compound $[\text{Ru}(\text{tpy})(\text{bpy})\text{Q}]^{2+}$.

3.2.4 Synthesis of Chloroquinoline Base

Chloroquine base (CQ) was produced using an adaptation of a modified published procedure.^{11,48} Chloroquine diphosphate (CQDP) (5 g, 9.69 mmol) was dissolved in 35 mL of DI (deionized) water. Concentrated ammonia solution (7 mL) was added dropwise to the clear solution turning it a milky white. After sonication, the drug was extracted twice using chloroform (200 mL), followed by a diethyl ether extraction (50 mL). After removing both solvents via rotary evaporation an oil remained in the flask. This oil was redissolved in a minimum amount of acetonitrile (5 mL) and sonicated causing a white powder to precipitate. The white powder was collected and washed with additional acetonitrile (10 mL) and dried under gentle N₂ flow. Yield: 2.90g (94%). ¹H NMR (400 MHz, *methanol-d*₄) δ (ppm): 8.33 (d, J = 5.72 Hz, 1H), 8.18 (d, J = 9.04 Hz, 1H), 7.77 (d, J = 2.12 Hz, 1H), 7.39 (dd, J = 9.04, 2.20 Hz, 1H), 6.56 (d, J = 5.80 Hz, 1H), 3.83 (m, J = 5.16 Hz, 1H), 2.54 (q, J = 7.24 Hz, 4H), 2.49 (t, J = 7.62 Hz, 2H), 1.79-1.55 (m, 4H), 1.32 (d, J = 6.40 Hz, 3H), 1.01 (t, J = 7.18 Hz, 6H). The ¹H NMR assignments shown in Figure 3.13 are consistent with the spectrum of 99% pure, purchased CQ and literature.^{11,42}

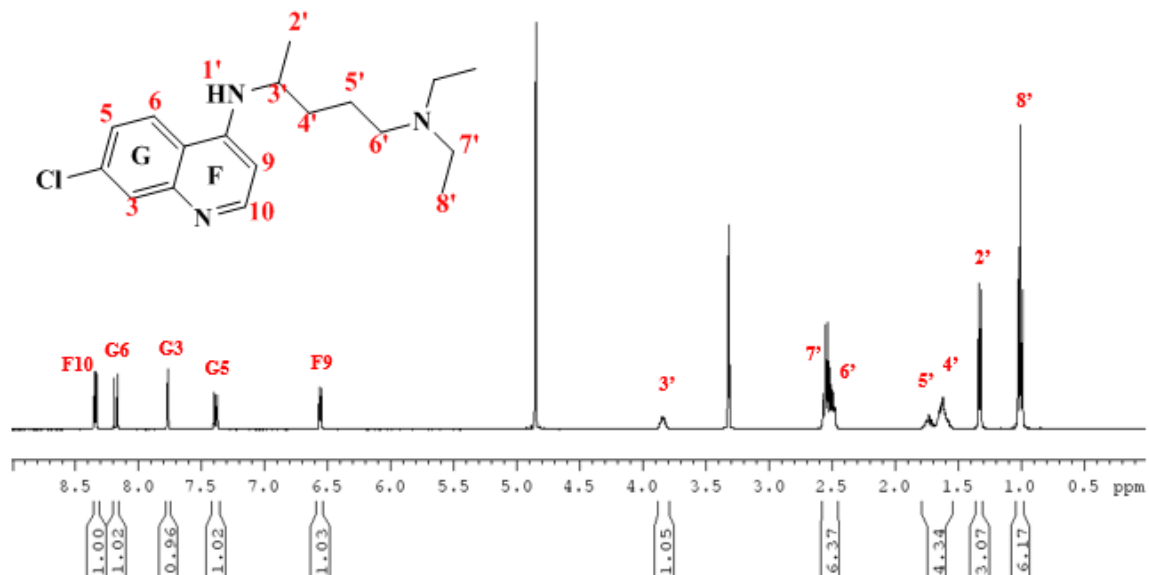


Figure 3.13 ^1H NMR spectrum (400 MHz, *methanol-d*₄): and proton assignments of Chloroquine base.

3.2.5 Synthesis of $[\text{Ru}(\text{tpy})(\text{bpy})(\text{CQ})][\text{PF}_6]_2$

$[\text{Ru}(\text{tpy})(\text{bpy})(\text{CQ})][\text{PF}_6]_2$ was synthesized and purified via a modified version of the previously described procedure for $[\text{Ru}(\text{tpy})(\text{bpy})(\text{Q})][\text{PF}_6]_2$. Thus, 61.2 mg (0.09 mmol) of $[\text{Ru}(\text{tpy})(\text{bpy})\text{Cl}][\text{PF}_6]$, 23.1 mg (0.09 mmol) of AgOTf, and 15 mL of deareated EtOH (via N_2 bubbling) were added to a 50 mL round bottom flask, sonicated, covered in foil and heated at reflux for 1 hour under N_2 . AgCl was removed by filtering the solution hot through celite. Chloroquine ligand (436.4 mg, 1.36 mmol) was dissolved in 10 mL of N_2 deareated EtOH was added to the filtrate and refluxed for 19 hours (Figure 3.14). The orange-red solution was filtered through celite, reduced in volume, and added dropwise to stirring ether three times to remove excess ligand. The product was then converted to the

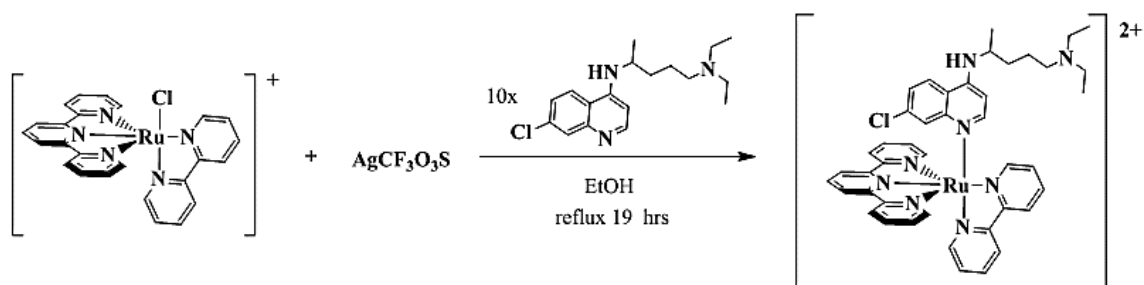


Figure 3.14 Synthetic scheme for $[\text{Ru}(\text{tpy})(\text{bpy})\text{CQ}][\text{PF}_6]_2$.

$[\text{PF}_6]^-$ salt by dissolving the dark orange powder in acetone and adding dropwise to NH_4PF_6 aqua slurry, filtered via celite, eluded with acetone and dried via rotary evaporation to yield a dark orange-black crystalline powder. Yield: 79.4 mg (79 %). ^1H NMR and residual coupled ^{13}C (600 MHz, *methanol-d*₄) δ (ppm): 9.09 (dd, $J = 11.56, 5.04$ Hz, 1H, $^{13}\text{C} = 155.36$), 8.91 (d, $J = 8.12$ Hz, 1H, $^{13}\text{C} = 125.84$), 8.81 (d, $J = 8.32$ Hz, 1H, $^{13}\text{C} = 125.67$), 8.74 (d, $J = 9.24$ Hz, 1H, $^{13}\text{C} = 127.02$), 8.64 (d, $J = 8.08$ Hz, 1H, $^{13}\text{C} = 125.42$), 8.52 (dd, $J = 8.26, 2.42$ Hz, 1H, $^{13}\text{C} = 124.81$), 8.43 (d, $J = 5.19$ Hz, 1H, $^{13}\text{C} = 155.92$), 8.40 (td, $J = 7.64, 1.48$ Hz, 1H, $^{13}\text{C} = 139.30$), 8.33 (dd, $J = 7.64, 1.29$ Hz, 1H, $^{13}\text{C} = 125.35$), 8.23 (t, $J = 8.14$ Hz, 1H, $^{13}\text{C} = 137.32$), 8.10-8.09 (m, 3H, $^{13}\text{C} = 125.87, 139.97, 128.05$), 7.91-7.86 (m, 3H, $^{13}\text{C} = 139.92, 138.62, 128.98$), 7.56 (d, $J = 5.24$ Hz, 1H, $^{13}\text{C} = 153.23$), 7.45-7.30 (m, 4H, $^{13}\text{C} = 128.91, 129.69, 126.42, 152.60$), 7.16 (dd, $J = 6.82, 2.58$ Hz, 1H, $^{13}\text{C} = 155.04$), 7.12 (t, $J = 6.72$ Hz, 1H, $^{13}\text{C} = 128.37$), 6.33 (dd, $J = 12.83, 7.00$ Hz, 1H, $^{13}\text{C} = 102.03$), 3.68 (m, 1H, $^{13}\text{C} = 49.81$), 3.08 (m, 4H, $^{13}\text{C} = 48.41$), 2.98 (m, 2H, $^{13}\text{C} = 53.14$), 1.67 (m, 3H), 1.55 (m, 1H), 1.37 (d, $J = 8.29$ Hz, 3H, $^{13}\text{C} = 20.08$), 1.22 (t, $J = 7.77$ Hz, 6H, $^{13}\text{C} = 20.10$). The proton assignments and NMR spectrum are shown in Figure 3.15. These assignments were determined using the three 2D NMR experiments described

previously, COSY (Figure 3.16), HSQC (Figure 3.17), and HMBC (Figure 3.18). Furthermore, HSQC was used to determine the residual carbon chemical shifts, listed in Table 3.2, and for HMBC the NMR probe was calibrated to detect 3J heteronuclear 1H - ^{13}C couplings in the aromatic region and 2J heteronuclear 1H - ^{13}C couplings in the aliphatic region. ESI MS: m/z 405.11, corresponding to $[Ru(tpy)(bpy)CQ]^{2+}$ (Figures 3.19 and 3.20).

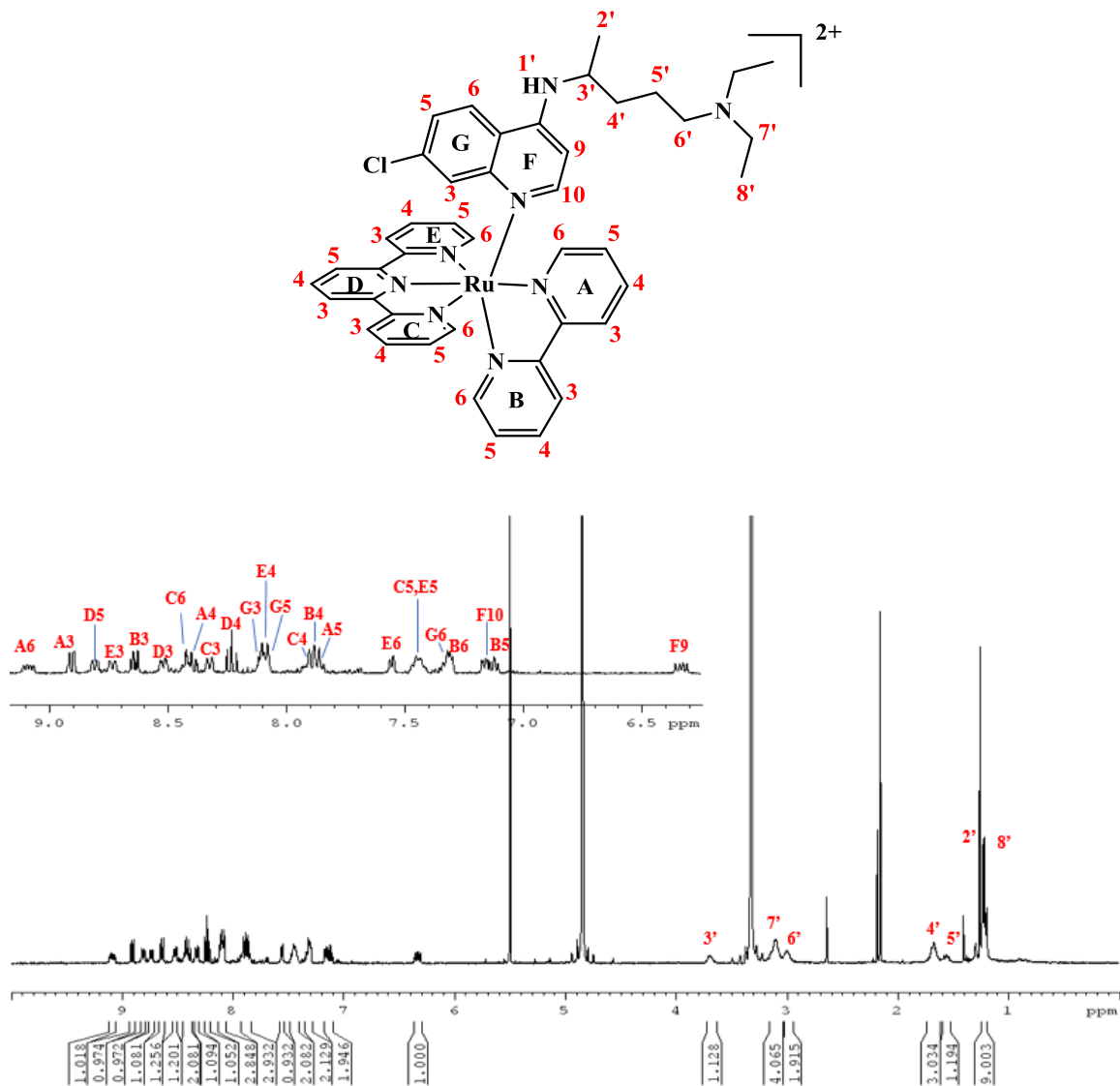


Figure 3.15 ^1H NMR spectrum (600 MHz, $\text{methanol-}d_4$) and proton peak assignments for $[\text{Ru}(\text{tpy})(\text{bpy})\text{CQ}][\text{PF}_6]_2$.

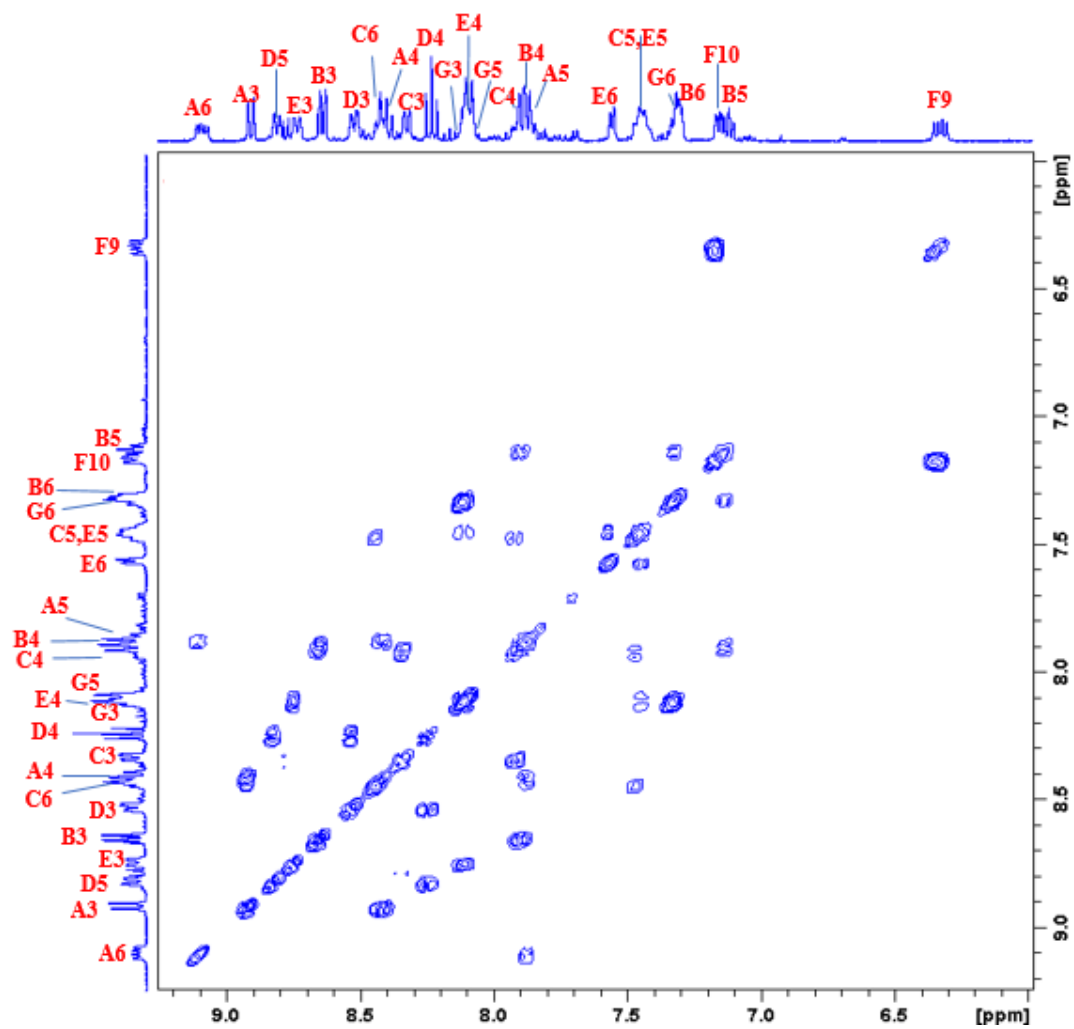


Figure 3.16 ^1H - ^1H 2D COSY NMR of $[\text{Ru}(\text{tpy})(\text{bpy})(\text{CQ})]^{2+}$ (400 MHz, *methanol-d*₄).

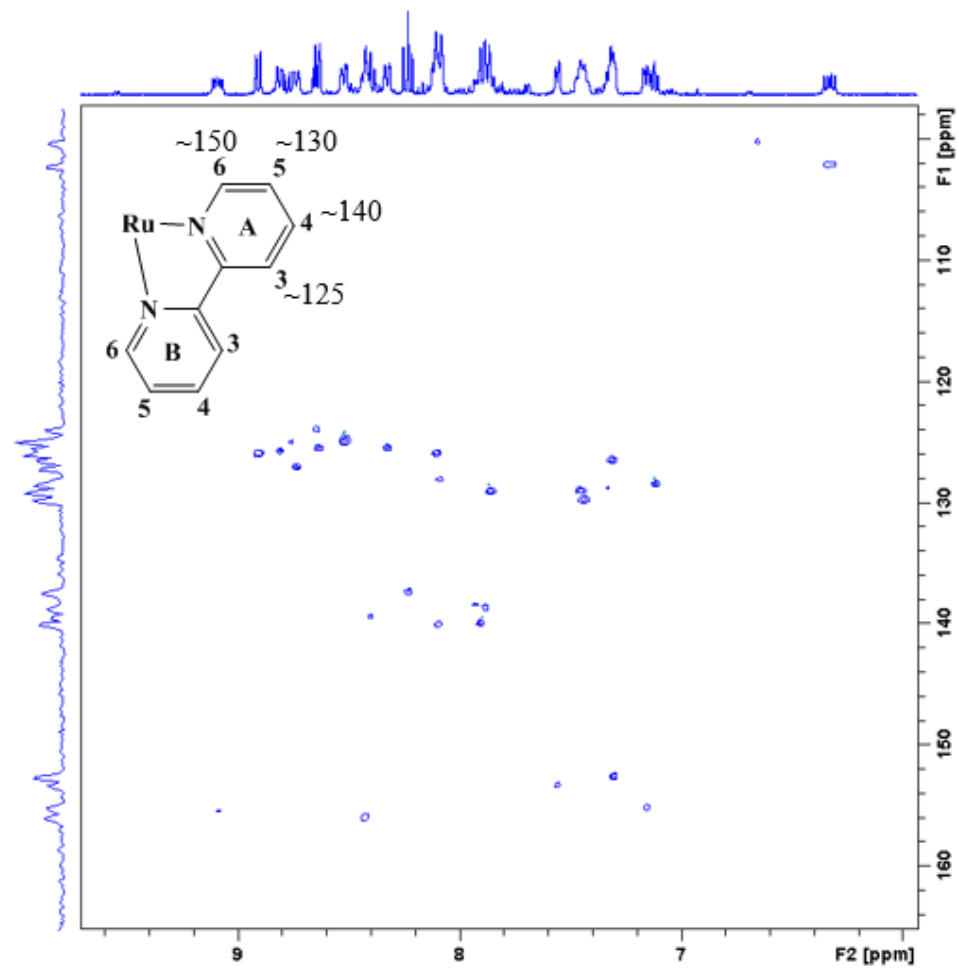


Figure 3.17 ^1H - ^{13}C 2D HSQC NMR of $[\text{Ru}(\text{tpy})(\text{bpy})(\text{CQ})]^{2+}$ (600 MHz, *methanol-d*₄).

Table 3.2 ^1H and ^{13}C chemical shifts and multiplicity of $[\text{Ru}(\text{tpy})(\text{bpy})(\text{CQ})]^{2+}$ from HSQC (600 MHz, *methanol-d*₄).

Label	Multiplicity	^1H (ppm)	^{13}C (ppm)
A6	dd	9.09	155.4
A3	d	8.91	125.9
D5	d	8.881	125.7
E3	d	8.74	127.0
B3	d	8.64	125.4
D3	dd	8.52	124.8
C6	d	8.43	155.9
A4	td	8.40	139.3
C3	dd	8.33	125.4
D4	t	8.23	137.3
G3	m	8.10	125.9
E4	m	8.10	140.0
G5	m	8.09	128.0
C4	m	7.91	139.9
B4	m	7.88	138.6
A5	m	7.86	129.0
E6	d	7.56	153.2
C5	m	7.45	128.8
E5	m	7.44	129.6
G6	m	7.31	126.3
B6	m	7.30	152.6
F10	dd	7.16	155.0
B5	t	7.12	128.3
F9	dd	6.33	102.0
3'	m	3.68	49.8
7'	m	3.08	48.4
6'	m	2.98	53.1
4'	m	1.67	-
5'	m	1.55	-
2'	d	1.37	20.0
8'	t	1.22	20.1

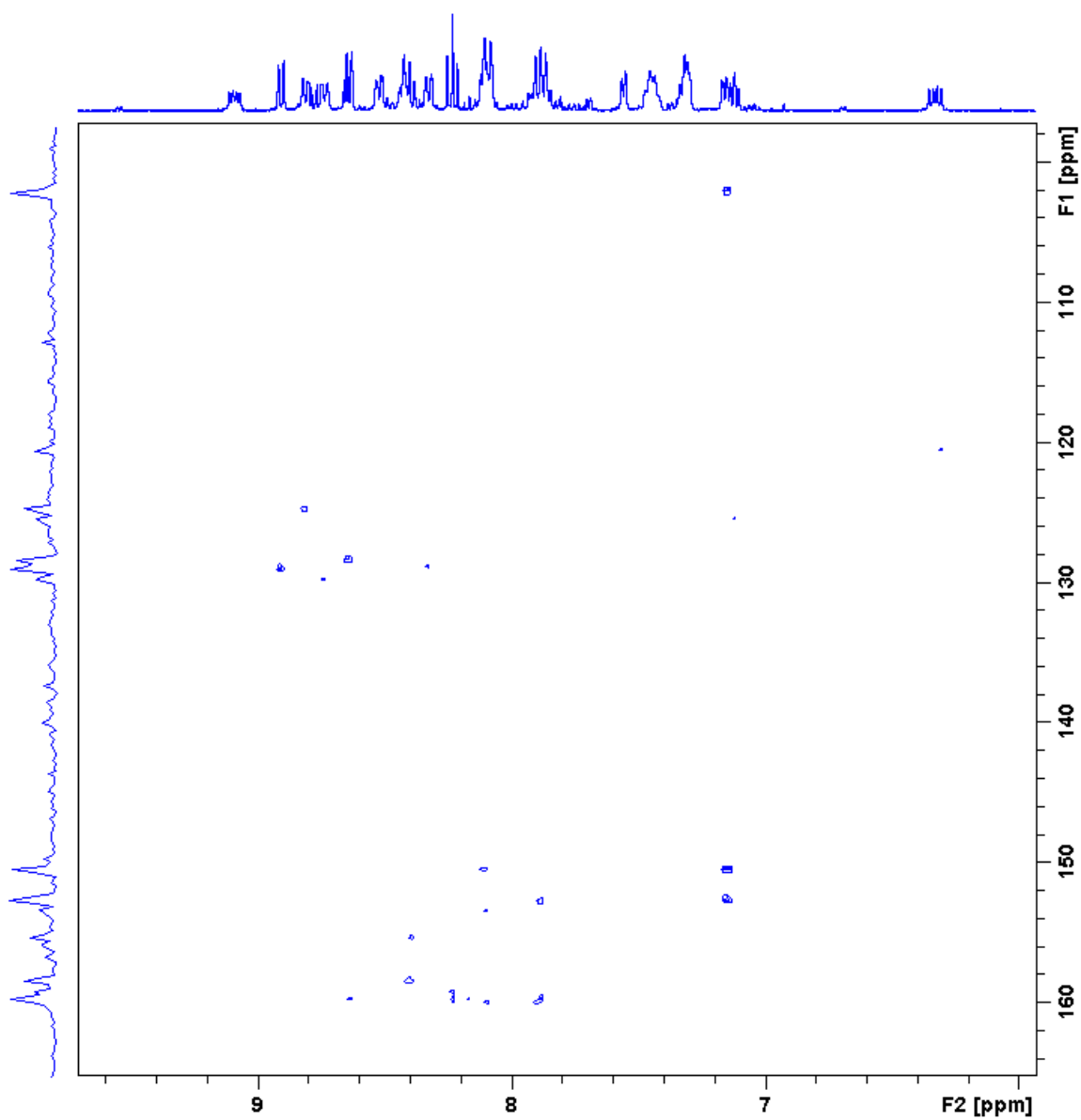


Figure 3.18 ^1H - ^{13}C 2D HMBC NMR of the ^3J aromatic couplings and ^2J aliphatic couplings of $[\text{Ru}(\text{tpy})(\text{bpy})(\text{CQ})]^{2+}$ (600 MHz, *methanol- d_4*).

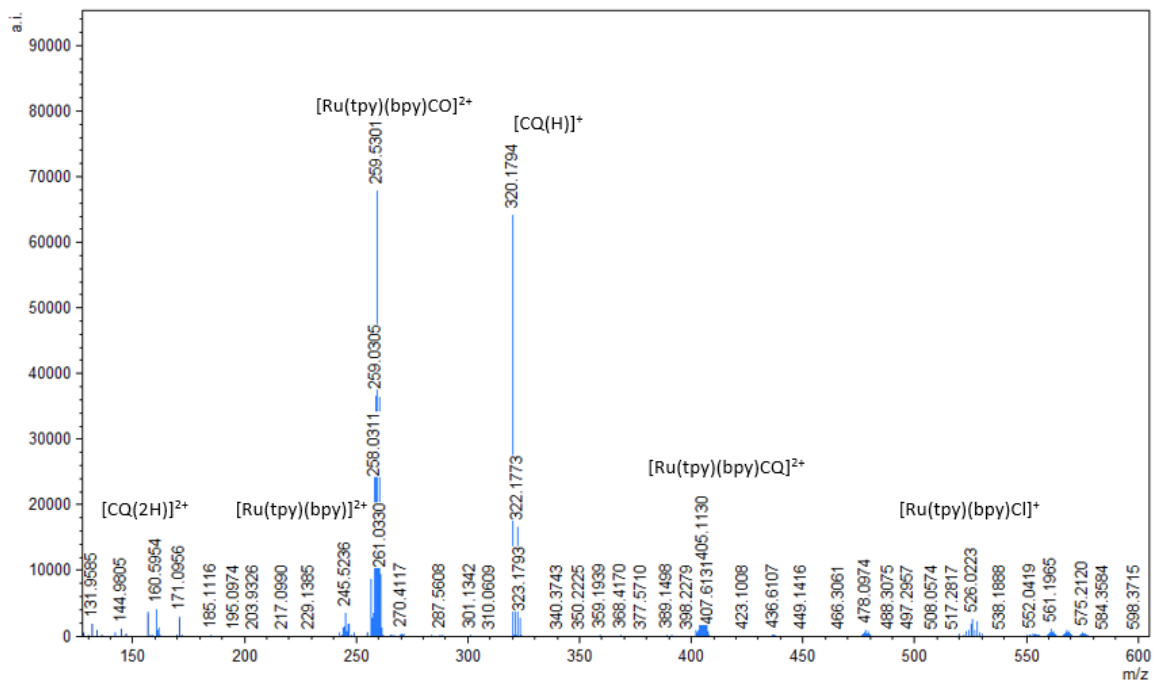


Figure 3.19 ESI-MS of $[\text{Ru}(\text{tpy})(\text{bpy})\text{CQ}]^{2+}$ in acetonitrile.

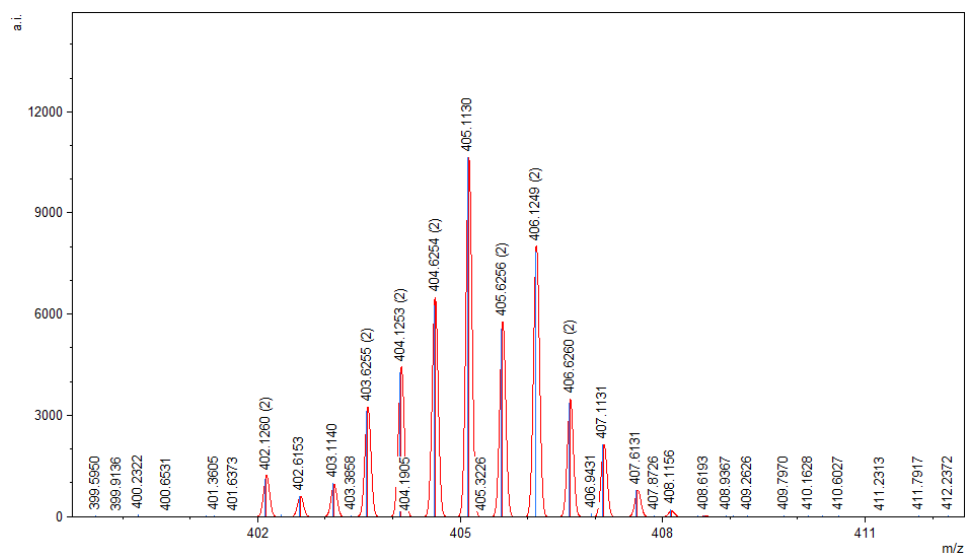


Figure 3.20 Expanded view of ruthenium isotopic pattern in mass spectrum of compound $[\text{Ru}(\text{tpy})(\text{bpy})\text{CQ}]^{2+}$.

3.3 Instrumentation

A 400 MHz Bruker NMR spectrometer was used to obtain both 1D ^1H NMR and 2D ^1H - ^1H COSY spectra, and a 600MHz Bruker NMR spectrometer was used to acquire 2D ^1H - ^{13}C HSQC and ^1H - ^{13}C HMBC spectral data. Topspin v 3.5 and 3.5 pl7 software were used to determine chemical shift (in ppm), integration, and nuclear coupling results. Mass spectra were measured using an Bruker MicroTOF spectrometer equipped with Agilent 1200 LC, using an electrospray ionization (ESI) ion source. Bruker Daltonics DataAnalysis software was used to correlate the fractions eluted from the LC to an isotopic pattern to be analyzed using mMass v 5.0 software. Electronic absorption spectra were collected on a Hewlett-Packard diode array spectrophotometer (Cary 8453 and Cary 8454) from Agilent Technologies equipped with Agilent Cary 8454 Win System software. All electronic absorption and photolysis samples were contained in a 1x1 cm² quartz cuvette, capped, and parafilm. A 150 W Xe arc lamp from Photon Technology International with an LPS-220 power supply and LPS-221 Arc Lamp Igniter was used as the light source to conduct photolysis experiments. Irradiation wavelengths were selected by using a long-pass colored glass filters (Melles Griot) or a Thor Labs 500 nm band pass filter model FB500-10 with a FWHM = 10 nm between the lamp and the sample. Royal blue LUXEON Rebel LED light sources ($\lambda_{\text{irr}} \geq 447 \pm 10$ nm) were used as the irradiation source for the NMR photolysis experiments.

3.4 Photochemical Methods

3.4.1 Extinction Coefficients

The measurement of extinction coefficients is useful for comparing the absorptivities of differing compounds, as well as in calculating their ligand dissociation quantum yields. A stock solution was prepared by dissolving at least 10.0 mg of [Ru(tpy)(bpy)X][PF₆]₂ (X = CQ, Q) sample in a 50 mL volumetric flask using acetone (or distilled acetonitrile). In a 1x1 cm² quartz cuvette cell 2.00 mL of pure solvent was added, which served as the blank. 250 μL of the stock solution containing the compound of interest was added to the original 2.00 mL, mixed, and an absorption spectrum was recorded. Four additional 250 μL aliquots of stock were added to the cuvette, mixed, and recorded individually for a total of five UV-Vis spectra with differing concentrations. This procedure was repeated in triplicate with three different sets of stock solution. The extinction coefficient was then calculated by plotting Beer's Law (equation 1) at a particular wavelength and determining the slope of the linear fit. In equation 1; A is the absorbance value at λ_{max} of the MLCT, ε is the extinction coefficient, b is the length of the unit cell (1 cm), and C is the concentration of the sample.

$$A = \epsilon b C \quad (1)$$

3.4.2 UV-Vis Photolysis

For photolyses conducted in water, less than 5 mg of [Ru(tpy)(bpy)Q][PF₆]₂ or [Ru(tpy)(bpy)CQ][PF₆]₂ was dissolved in a small volume of acetone before adding to

water, to facilitate solvation. Samples were prepared by pipetting 2.00 mL of DI water into a quartz cuvette, followed by 100 μ L acetone containing each dissolved compound, resulting in solutions with less than 5% acetone by volume. For the photolyses conducted in acetonitrile, the samples were dissolved directly into deaerated, by bubbling with N_2 for 1 hour, acetonitrile and 2.00 mL of the stock solution was pipetted into the sample cuvette. Photolysis reactions were carried out using a 150 W Xe arc lamp passing through a 395 nm long pass filter. Because of the long nature of the experiment blanking on air instead of solvent was necessary before each reading. Electronic spectral measurements were taken after irradiating for incremental amounts of time, overlaid, and baseline corrected to observe the changes in the absorption spectrum over time. The photolyses were considered complete when the last two spectra were identical, no longer displaying a noticeable change in absorption after additional irradiation time.

3.4.3 *Quantum Yields*

The intensity of the incident light was measured and calculated via standard ferrioxalate actinometry. Ferric oxalate has a well characterized sensitive photochemical reaction through which, upon irradiation, the iron(III) is reduced to iron(II). The addition of 1,10-phenanthroline ligand to the irradiated solution results in the exclusive coordination of iron(II) forming $[Fe(phen)_3]^{2+}$, which absorbs in the visible region allowing the reaction to be monitored by UV-Vis spectroscopy. The actinometry measurements of the iron oxalate photoreaction were recorded in triplicate for three different irradiation time points: 1 min, 2 mins, and 4 mins, including one dark reaction. After allowing the ten sample

solutions to incubate for an hour in the dark, the electronic absorption spectra were measured and recorded. The intensity of the lamp was determined using equation 2,⁶⁶ and the known quantum yield of the iron oxalate reaction for the closest appropriate wavelength; where A is the measured absorbance at 510 nm, ϵ is the extinction coefficient of $[\text{Fe}(\text{phen})_3]^{2+}$ ($1.11 \times 10^4 \text{ M}^{-1} \text{ cm}^{-1}$), d is the path length of the cuvette, ϕ_λ is the known quantum yield of iron oxalate (0.90) at 502 nm, t is the irradiation time, and V_1 , V_2 , V_3 are the volumes for the irradiated actinometer used, actinometer irradiated in liters, and the total sample volume respectively.

$$I = \frac{AV_2V_3}{\epsilon d \phi_\lambda t V_1} \quad (2)$$

The absorption of each compound at the irradiation wavelength was measured below 1.0 A.U. upon excitation at 500 nm. All solutions containing the sample compounds $[\text{Ru}(\text{tpy})(\text{bpy})\text{Q}][\text{PF}_6]_2$ and $[\text{Ru}(\text{tpy})(\text{bpy})\text{CQ}][\text{PF}_6]_2$ were degassed using N_2 for 30 minutes in the dark prior to photolysis. The samples were irradiated and monitored at 500 nm until a 5-10% change in absorbance was observed. The photolysis for each compound was carried out in triplicate before calculating the resulting quantum yield. Equation 3 and 4 were used to determine the quantum yield of ligand dissociation, where $[\text{R}]_0$ is the molar concentration of the reactant at time zero, $[\text{R}]_t$ is the molar concentration of the reactant at the end of the irradiation time, V is the total sample volume in the cuvette in liters, N_A is Avogadro's number (omitted if the flux is expressed in Einsteins), I is the lamp flux determined using actinometry, and t is the total irradiation time in minutes. The value f_m represents the fraction of photons absorbed as described in equation 3, where A_0 and A_t are the initial and final absorbance values after time t respectively.

$$f_m = \frac{(1-10^{A_0})+(1-10^{A_t})}{2} \quad (3)$$

$$\phi = ([R]_0 - [R]_t) \times \frac{(V)N_A}{(I)t} \times \frac{1}{f_m} \quad (4)$$

3.4.4 NMR Photolysis

A combination of the NMR spectroscopy with photolysis can be a useful technique for the observation and structure determination of transient products of photochemical reactions, as well as providing further verification of the chemical structure of the final photochemical product.⁶⁷ Both the complexes [Ru(tpy)(bpy)Q][PF₆]₂ and [Ru(tpy)(bpy)CQ][PF₆]₂ were monitored using ¹H NMR experiments in deuterated acetonitrile. The samples were irradiated for using blue LEDs ($\lambda_{\text{irr}} \geq 447 \pm 10$ nm) with the NMR tube placed directly between two LEDs for various lengths of time and followed by NMR. Differences in peak intensities over irradiation time indicate a photochemical change, with reactant peaks decreasing while new product peaks appear in the spectrum. The photolysis was deemed complete after there was no change in peak intensity of chemical shift after 12 hours of irradiation.

Chapter 4: Results and Discussion

4.1 Electronic Absorption

The electronic absorption spectrum and extinction coefficient of $[\text{Ru}(\text{tpy})(\text{bpy})(\text{py})]^{2+}$ have been previously reported in various solvents.^{35,65} The absorption spectra in the ultraviolet-visible regions were obtained separately for $[\text{Ru}(\text{tpy})(\text{bpy})(\text{Q})]^{2+}$ and $[\text{Ru}(\text{tpy})(\text{bpy})(\text{CQ})]^{2+}$ in acetone. The electronic absorption spectrum of each complex was overlaid onto that of $[\text{Ru}(\text{tpy})(\text{bpy})(\text{py})]^{2+}$ for comparison and the resulting plots are shown in Figure 4.1. All three ground state absorption spectra show ligand centered (LC) $^1\pi\pi^*$ transitions with maxima in the UV region at ~ 300 nm that primarily corresponds to the tpy ligand.^{68,69} This type of electronic transition is also coined as an intra-ligand (IL) transition, and bpy is also known to contribute to this absorption in the UV.³⁶ The peaks at 358 nm and 364 nm for $[\text{Ru}(\text{tpy})(\text{bpy})(\text{Q})]^{2+}$ and $[\text{Ru}(\text{tpy})(\text{bpy})(\text{CQ})]^{2+}$ respectively, are thought to be LC electronic transitions centered on the quinoline and chloroquine ligands, as the ligands absorb in this region on their own. The lowest energy transition in $[\text{Ru}(\text{tpy})(\text{bpy})(\text{py})]^{2+}$ is centered at 468 nm which has previously been assigned as arising from $\text{Ru} \rightarrow \text{tpy}$ $^1\text{MLCT}$.³⁴ Similarly, it is thought that the quinoline and chloroquine bound complexes exhibit singlet metal to ligand charge transfer transitions from the ruthenium t_{2g} state to the π^* orbital on the tpy ligand, with maxima at 469 nm and 478 nm in acetone respectively.

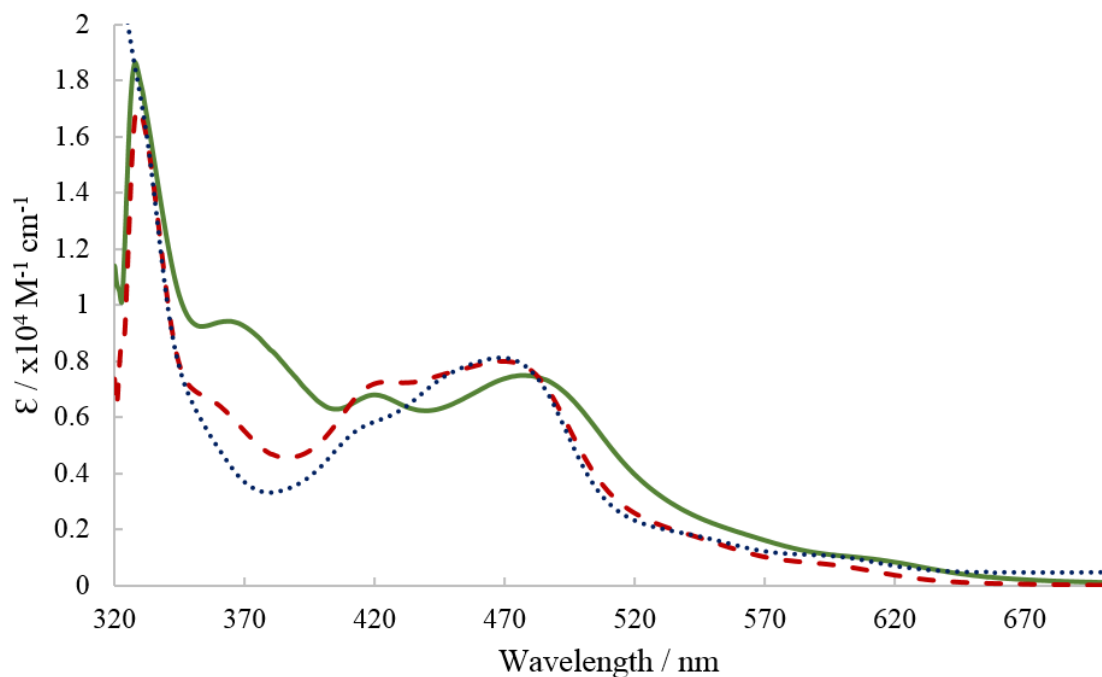


Figure 4.1 Electronic absorption spectra of $[\text{Ru}(\text{tpy})(\text{bpy})(\text{CQ})]^{2+}$ (solid line), $[\text{Ru}(\text{tpy})(\text{bpy})(\text{Q})]^{2+}$ (dashed line), and $[\text{Ru}(\text{tpy})(\text{bpy})(\text{py})]^{2+}$ (dotted line) in acetone.

The absorption maxima and their respective extinction coefficients for the two new complexes were compared in acetone and acetonitrile. The λ_{max} of all three compounds in CH_3CN demonstrate a negligible hypsochromic (blue) shift compared to measurements in $(\text{CH}_3)_2\text{CO}$, rendering the two spectra virtually identical. This may be due to the similarity in polarity of the two solvents, acetone's dielectric constant being 5.1 and that of acetonitrile 5.8. The MLCT absorption maxima observed for each of the complexes are similar across solvents. As shown in Table 4.1, when comparing the extinction coefficients measured in acetonitrile versus acetone the values are within error of one another.

Table 4.1 Absorption maximum and extinction coefficients of [Ru(tpy)(bpy)L]²⁺ compounds in acetone and acetonitrile.

Complex	(CH ₃) ₂ CO	CH ₃ CN
	$\lambda_{\text{abs}}/\text{nm}$ ($\epsilon/\text{M}^{-1}\text{cm}^{-1}$)	$\lambda_{\text{abs}}/\text{nm}$ ($\epsilon/\text{M}^{-1}\text{cm}^{-1}$)
[Ru(tpy)(bpy)(py)] ²⁺	468 (8120) ^[a]	467 ^[b]
[Ru(tpy)(bpy)(Q)] ²⁺	469 (8000 ± 240)	467 (8100 ± 92)
[Ru(tpy)(bpy)(CQ)] ²⁺	478 (7300 ± 290)	475 (7100 ± 320)

^[a] Reference (34) ^[b] Ref (65)

In general, the drug bound complex [Ru(tpy)(bpy)(CQ)]²⁺ is ~9 nm red-shifted in both listed solvents compared to the pyridine and quinoline bound complexes. However, the absorbance maxima for [Ru(tpy)(bpy)(py)]²⁺ and [Ru(tpy)(bpy)(Q)]²⁺ match in both solvents, ~469 nm in acetone and 467 nm in acetonitrile. Furthermore, their respective extinction coefficients in acetone 8100 M⁻¹cm⁻¹ and 8000 M⁻¹cm⁻¹ are within error of one another. For the chloroquine bound complex, the ϵ value is lower than its simpler derivatives measuring 7300 ± 290 M⁻¹cm⁻¹ in acetone and 7100 ± 320 M⁻¹cm⁻¹ in acetonitrile. This slight hypochromatic effect indicates that [Ru(tpy)(bpy)(CQ)]²⁺ does not absorb 450-500 nm light as efficiently as its quinoline counterpart.

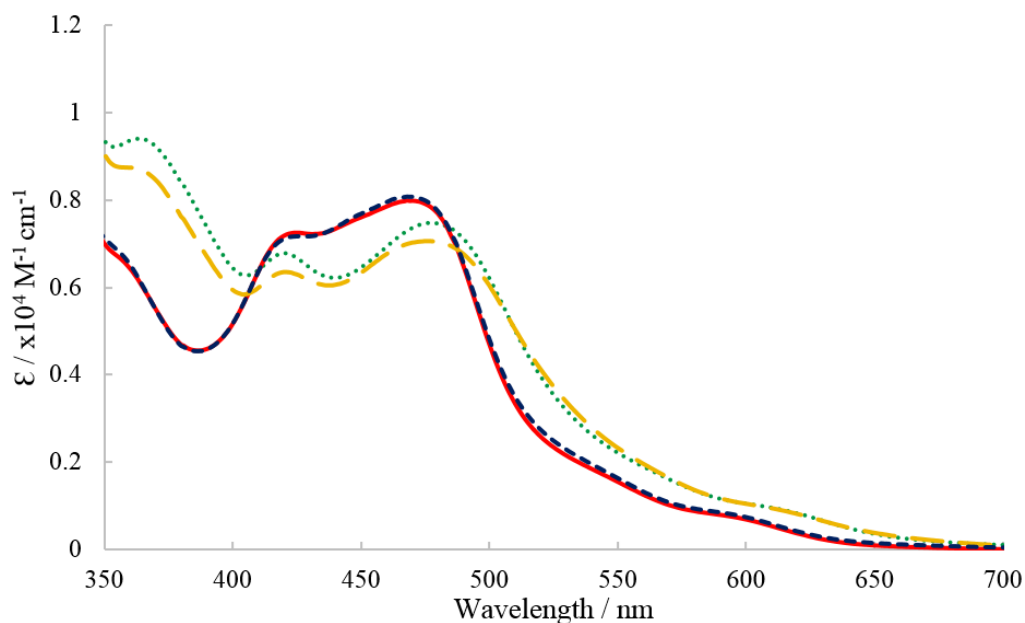


Figure 4.2 Electronic ground state absorption in different solvents for $[\text{Ru}(\text{tpy})(\text{bpy})(\text{Q})]^{2+}$ (solid red line) and $[\text{Ru}(\text{tpy})(\text{bpy})(\text{CQ})]^{2+}$ (dotted green line) in acetone, and $[\text{Ru}(\text{tpy})(\text{bpy})(\text{Q})]^{2+}$ (small dashed blue line), $[\text{Ru}(\text{tpy})(\text{bpy})(\text{CQ})]^{2+}$ (large dashed yellow line) in acetonitrile.

4.2 Photolysis in Acetonitrile

The photolysis of $[\text{Ru}(\text{tpy})(\text{bpy})(\text{Q})]^{2+}$ in acetonitrile results in the exchange of the quinoline ligand for a solvent molecule, resulting in the formation of $[\text{Ru}(\text{tpy})(\text{bpy})(\text{CH}_3\text{CN})]^{2+}$. The quinoline is replaced by a coordinating CH_3CN solvent molecule as shown in Figure 4.3. The photolysis was conducted in distilled, deaerated acetonitrile irradiated at 395 nm over the course of 12 hours. The evolution of the photochemical process is depicted in Figure 4.4, alongside its respective dark control. In order for these novel complexes to be relevant for PDT applications, they must demonstrate dark stability in solution. After a brief incubation period of 1 hour at room temperature, both $[\text{Ru}(\text{tpy})(\text{bpy})(\text{Q})]^{2+}$ and $[\text{Ru}(\text{tpy})(\text{bpy})(\text{CQ})]^{2+}$ are stable in acetonitrile for up to 24

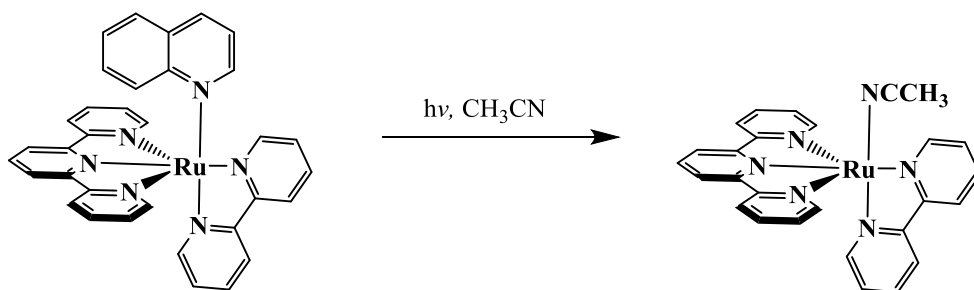


Figure 4.3 Photoproduct scheme, solvent substitution of quinoline ligand in acetonitrile upon irradiation.

hours. The photoproduct after irradiation was characterized and confirmed as $[\text{Ru}(\text{tpy})(\text{bpy})(\text{CH}_3\text{CN})]^{2+}$ by UV-Vis and proton NMR spectroscopies, consistent with previously reported characterizations.^{35,65} As the reactant undergoes ligand dissociation, a hypsochromic effect is observed in the absorption spectrum indicated by the $^1\text{MLCT}$ state shifting to lower wavelengths and thus a higher energy. This shift is due to the increased ligand field splitting of the acetonitrile ligand compared to that of quinoline bound complex. Thus, the $^1\text{MLCT}$ electronic excited state of $[\text{Ru}(\text{tpy})(\text{bpy})(\text{Q})]^{2+}$ is more accessible at a lower energy than the excited state of the photoproduct.

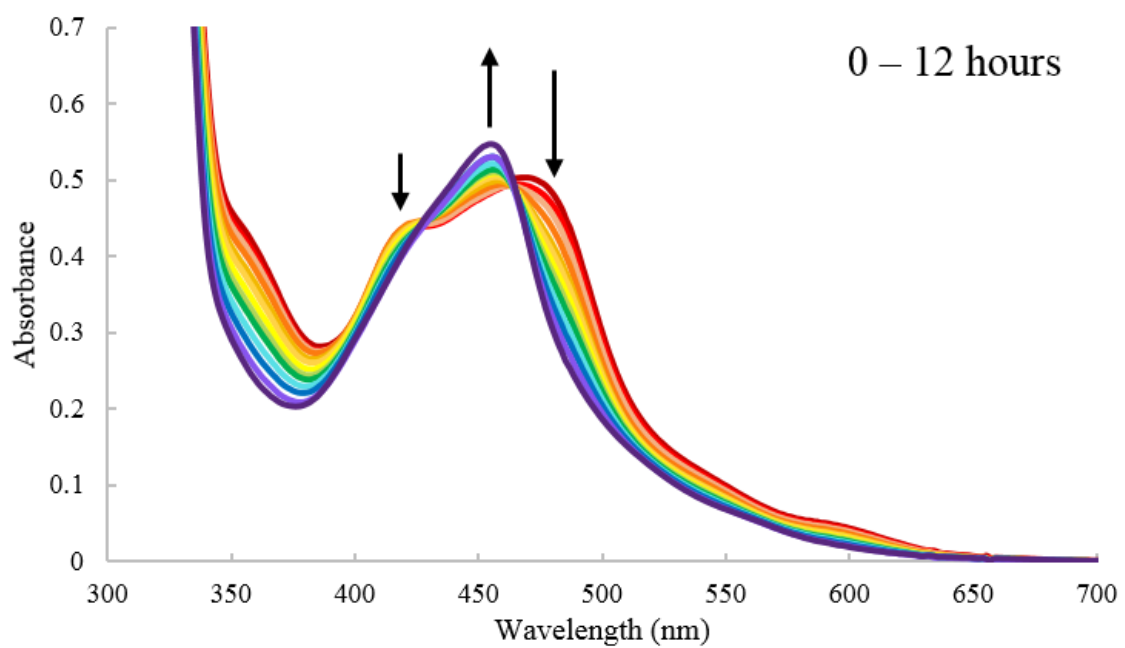
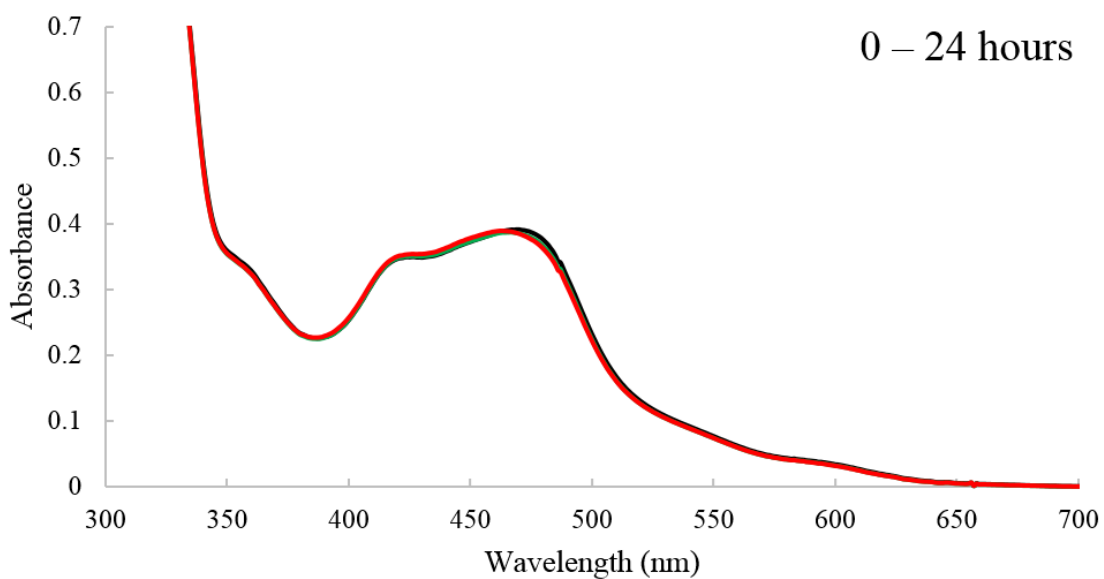


Figure 4.4 Changes to the electronic absorption spectrum of [Ru(tpy)(bpy)(Q)]²⁺ as a function of time when kept in the dark (top) and following irradiation with >395 nm light (bottom) in CH₃CN.

The photolysis reaction was followed via NMR spectroscopy to confirm the identity of the photoproduct. Due to the increase in solution concentration needed to acquire a clean NMR spectrum compared to an electronic absorption spectrum, it is expected that more time will elapse during the duration of the photolysis to reach complete conversion to the photoproduct. Thus, higher intensity royal blue LED lights were used instead of the standard 150W Xe arc lamp to speed up the photolysis of the NMR sample. Figure 4.5 illustrates the ^1H NMR spectra of $[\text{Ru}(\text{tpy})(\text{bpy})(\text{Q})]^{2+}$ changing into that of the

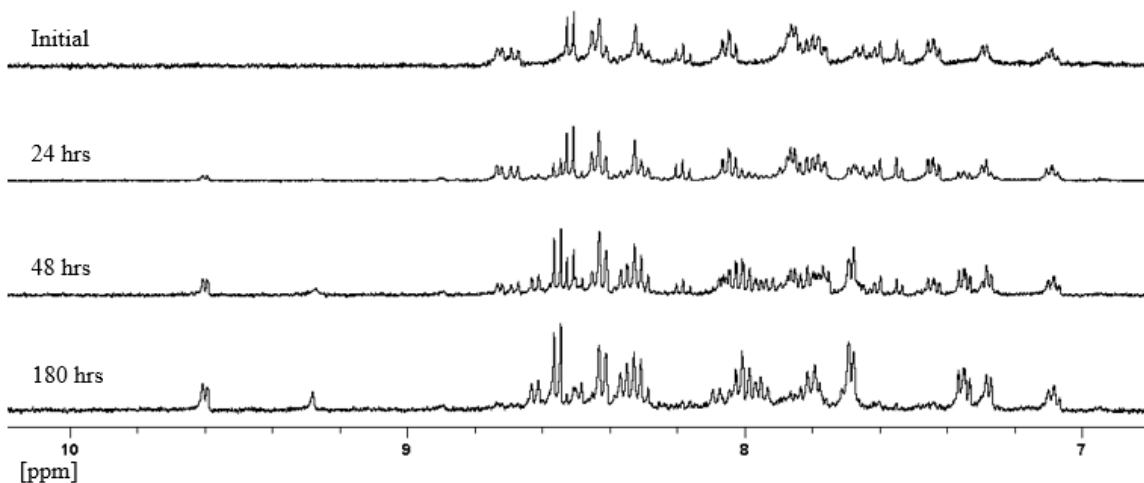


Figure 4.5 NMR Photolysis of $69 \mu\text{M}$ $[\text{Ru}(\text{tpy})(\text{bpy})(\text{Q})]^{2+}$ in CH_3CN using royal blue LUXEON Rebel LEDs as the light source ($\lambda_{\text{irr}} \geq 447 \pm 10 \text{ nm}$).

photoproduct over the course of the photolysis. The two highest field aromatic peaks at 8.72 and 8.69 ppm, localized on the bidentate ligand corresponding to previously labeled (Figure 3.7) protons A3 and A6 respectively, are the most informative due to their large shift. Notably, the A6 proton on the bpy, pointing towards the monodentate ligand, shifts ~ 0.9 ppm downfield from 8.69 to 9.60 ppm, while A3 shifts upfield ~ 0.2 ppm. The slight

chemical shift of the doublet corresponding to D3 and D5 protons on tpy's central pyridyl ring is another great indicator of the increase of $[\text{Ru}(\text{tpy})(\text{bpy})(\text{CH}_3\text{CN})]^{2+}$ in the sample over time. Initially the doublet is found at 8.51 ppm and decreases in intensity over the course of the photolysis, while a new doublet corresponding to the same protons on tpy for the photoproduct is observed increasing at 8.55. The disappearance of additional triplet peaks at 8.18 and 7.44 ppm, corresponding to protons D4, C5, and E5, indicate complete dissociation of the quinoline ligand after 180 hours. The aromatic peak integration, after complete conversion to the photoproduct, total 19; additionally, the overall NMR pattern also matches that of predicted solvent bound $[\text{Ru}(\text{tpy})(\text{bpy})(\text{CH}_3\text{CN})]^{2+}$, further confirming it as the identity of the product.

Much like its quinoline predecessor, the photolysis of $[\text{Ru}(\text{tpy})(\text{bpy})(\text{CQ})]^{2+}$ in acetonitrile results in the loss of the chloroquinoline drug ligand. As shown in Figure 4.6, the anti-parasitic drug is replaced by a coordinating solvent molecule. The photochemical reaction was monitored via UV-Vis photolysis of $[\text{Ru}(\text{tpy})(\text{bpy})(\text{CQ})]^{2+}$ in purged, distilled

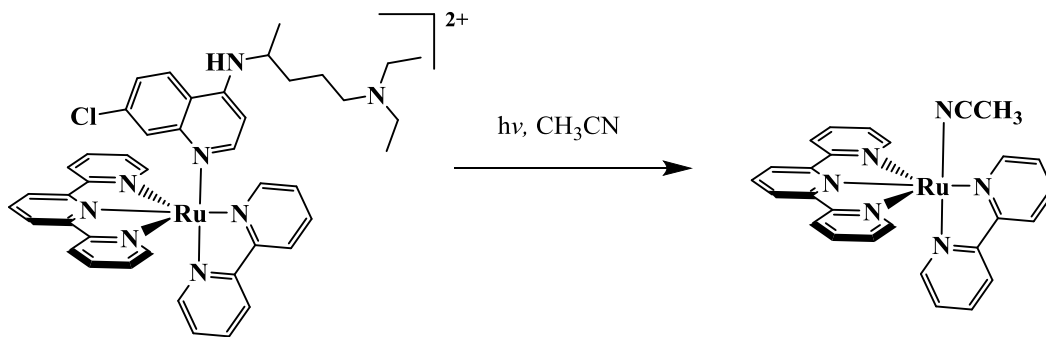


Figure 4.6 Photoproduct scheme, solvent substitution of chloroquinoline ligand in acetonitrile.

acetonitrile irradiated at 500 nm over all visible light during the course of 12 hours. The $^1\text{MLCT}$ state shifts to a higher energy; thus, as expected, a hypsochromic effect is observed when $[\text{Ru}(\text{tpy})(\text{bpy})(\text{CQ})]^{2+}$ undergoes ligand exchange with acetonitrile. Similarly to $[\text{Ru}(\text{tpy})(\text{bpy})(\text{Q})]^{2+}$ and its quinoline ligand, the increased ligand field splitting of the acetonitrile ligand compound causes the observed blue shift compared to that of the chloroquinoline bound ligand complex. This indicates that the $^1\text{MLCT}$ of $[\text{Ru}(\text{tpy})(\text{bpy})(\text{CQ})]^{2+}$ is lower in energy than the excited state of the solvent-bound photoproduct, a desirable feature for future PDT application.

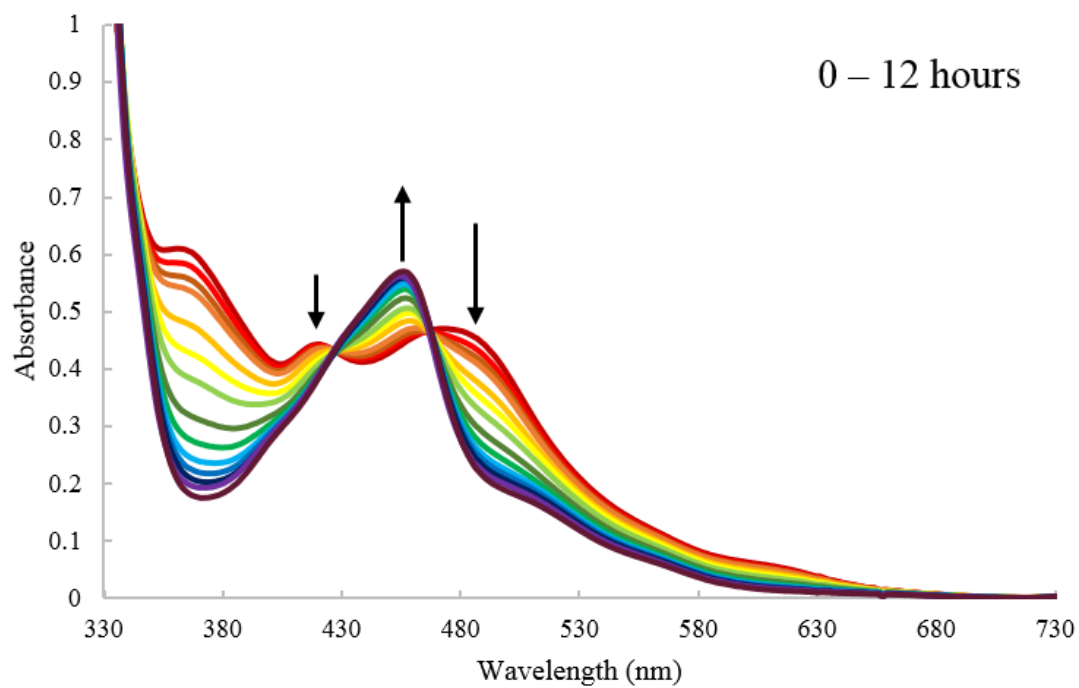
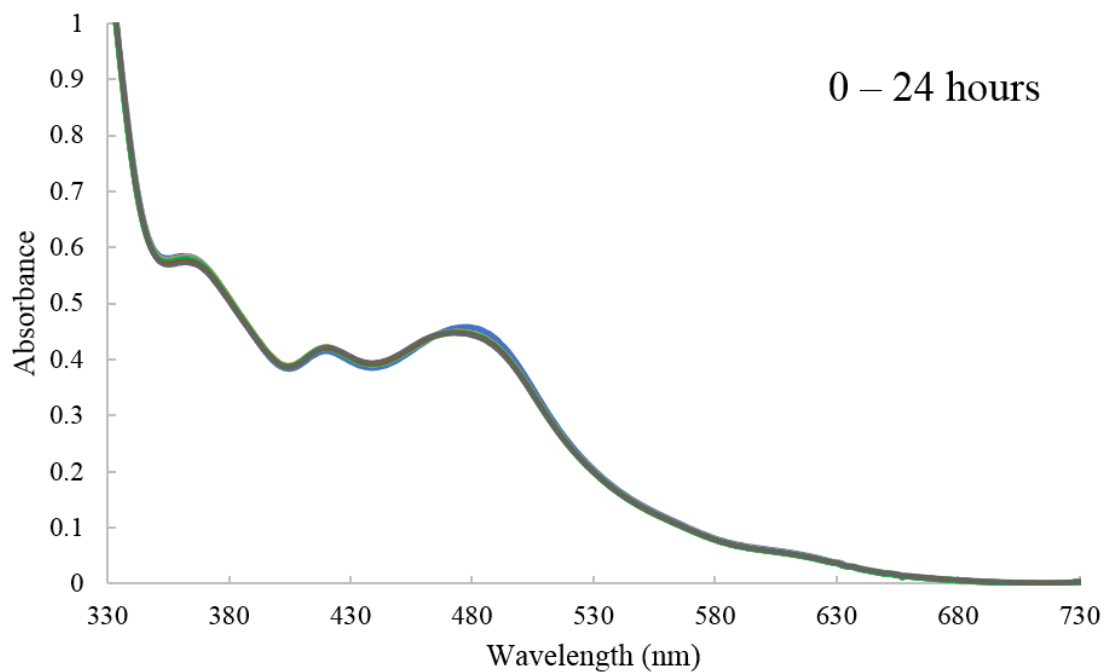


Figure 4.7 Changes to the electronic absorption spectrum of $[\text{Ru}(\text{tpy})(\text{bpy})(\text{CQ})]^{2+}$ as a function of time when kept in the dark (top) and following irradiation with >395 nm light (bottom) in CH_3CN .

In deuterated acetonitrile, the NMR photolysis of $[\text{Ru}(\text{tpy})(\text{bpy})(\text{CQ})]^{2+}$ was monitored after different irradiation times, illustrated below in Figure 5.8. Once again, after 48 hours and complete conversion to the photoproduct, the proton integration in the aromatic region and overall NMR pattern are consistent with the formation of $[\text{Ru}(\text{tpy})(\text{bpy})(\text{CH}_3\text{CN})]^{2+}$. The most notable proton shift is that of the furthest downfield

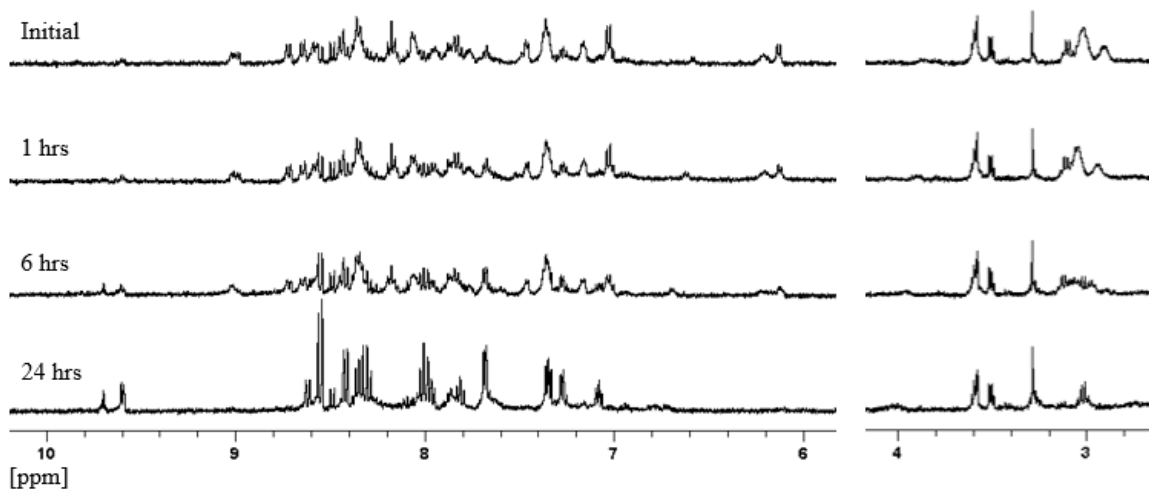


Figure 4.8 NMR Photolysis of $44 \mu\text{M}$ $[\text{Ru}(\text{tpy})(\text{bpy})(\text{CQ})]^{2+}$ in CH_3CN using royal blue LUXEON Rebel LEDs as the light source ($\lambda_{\text{irr}} \geq 447 \pm 10 \text{ nm}$).

doublet of doublets at 9.0 ppm, corresponding to the proton A6 (Figure 3.15) localized on the bidentate ligand closest to the chloroquine bound drug. This proton shifts ~ 0.6 ppm downfield to 9.60 ppm when solvent acetonitrile displaces the drug. The disappearance of proton F9, the doublet at 6.14 ppm, corresponding to a CQ aromatic proton further confirms complete conversion to photoproduct after 24 hours of irradiation. The gradual growth of the sharp doublet at 8.56 ppm over time, corresponding to the D3 and D5 tpy protons on

$[\text{Ru}(\text{tpy})(\text{bpy})(\text{CH}_3\text{CN})]^{2+}$, is another clear sign of the exchange of chloroquinoline. Comparatively, in $[\text{Ru}(\text{tpy})(\text{bpy})(\text{CQ})]^{2+}$ the D3 and D5 protons do not possess identical chemical shifts, due to the loss of symmetry when CQ is bound, and are found at 8.44 and 8.65 ppm respectively before irradiation. Additionally, in the aliphatic region from 2.86 to 3.14 ppm a pair of multiplets, corresponding to the six protons neighboring the imide on chloroquine (7' and 6'), are initially observed. As the photolysis progresses and the drug is free in solution, these multiplets converge around 3.0 ppm.

Quantum yields were calculated in order to quantitatively compare the relative efficiency of ligand exchange among the complexes. Using both 395 nm long pass filter and a 500 nm band pass filter, the ϕ_{500} for $[\text{Ru}(\text{tpy})(\text{bpy})(\text{Q})]^{2+}$ and $[\text{Ru}(\text{tpy})(\text{bpy})(\text{CQ})]^{2+}$ were determined to be $0.28(4) \times 10^{-3}$ and $0.32(3) \times 10^{-3}$ respectively. These values indicate a very inefficient dissociative process, however the complexes do exchange with solvent unlike previously reported $[\text{Ru}(\text{tpy})(\text{bpy})(\text{py})]^{2+}$, $\phi_{500} < 0.1 \times 10^{-3}$.³⁴ The long irradiation times necessary to release the quinoline and chloroquine drug would render them impractical complexes for PDT use on Leishmaniasis. Ideally the drug bound complex would be both stable in acetonitrile and would dissociate readily upon irradiation, thus possessing a large quantum yield, when irradiated. The simplest manner to increase drug release would be to replace bidentate ligand bpy with more sterically bulky ligands such as 6,6'-dimethyl-2,2'-bipyridine or 2,2'-biquinoline. This synthetic method of increasing ligand dissociation of the monodentate ligand via increase of bidentate steric bulk has proven effective for the $[\text{Ru}(\text{tpy})(\text{NN})(\text{py})]^{2+}$ (NN = bidentate ligand) series of compounds and should be expected to work similarly for $[\text{Ru}(\text{tpy})(\text{NN})(\text{CQ})]^{2+}$ type compounds.

Table 4.2 Ligand dissociation quantum yield comparison in CH₃CN at 500 nm.

Complex	ϕ_{irr} (500 nm)
[Ru(tpy)(bpy)(py)] ²⁺	<0.0001 ^[a]
[Ru(tpy)(bpy)(Q)] ²⁺	0.00028(4)
[Ru(tpy)(bpy)(CQ)] ²⁺	0.00032(3)

^[a] Reference (34)

4.3 Ligand Dissociation via Photoaquation

Although the complexes were shown to be dark stable in acetonitrile, water is the main medium proposed to administer these photosensitizers into biological systems. Typically gel electrophoresis and preliminary cell studies are also conducted in a water based or buffer medium. Therefore, to use [Ru(tpy)(bpy)(CQ)]²⁺ or [Ru(tpy)(NN)(CQ)]²⁺, for the treatment of cutaneous Leishmania it needs to exhibit dark stability in water for at least 24 hours. Thus, each compound was dissolved in water and kept in the dark for a day, recording UV-Vis at different time intervals throughout the incubation, ideally expecting to see little to no change in absorption spectra.

The changes to the electronic absorption spectra of [Ru(tpy)(bpy)(Q)]²⁺ and [Ru(tpy)(bpy)(CQ)]²⁺ are illustrated as a function of time kept in the dark or upon irradiation in Figures 4.9 and 4.10 respectively. Unfortunately, both control graphs show a dark reaction occurring within the first hours of incubation, with [Ru(tpy)(bpy)(CQ)]²⁺ demonstrating even less dark stability compared to [Ru(tpy)(bpy)(Q)]²⁺ in water. There is

an approximate 60% conversion to the aqua bound complex within only 2 hours of dissolving the drug compound in water. The photolyses for both $[\text{Ru}(\text{tpy})(\text{bpy})(\text{Q})]^{2+}$ and $[\text{Ru}(\text{tpy})(\text{bpy})(\text{CQ})]^{2+}$ were conducted in degassed, deionized water using a 395 nm long pass filter to irradiate the samples with all visible light. The preliminary results derived from the photolysis graphs indicate a more rapid drug release for both Q and CQ bound complexes in water compared to those previously discussed in acetonitrile, which would result in higher quantum yield values. However, these values would be considered 'false' high quantum yields given that this increase in conversion to photoproduct is likely the result of both a light and dark reaction simultaneously taking place.

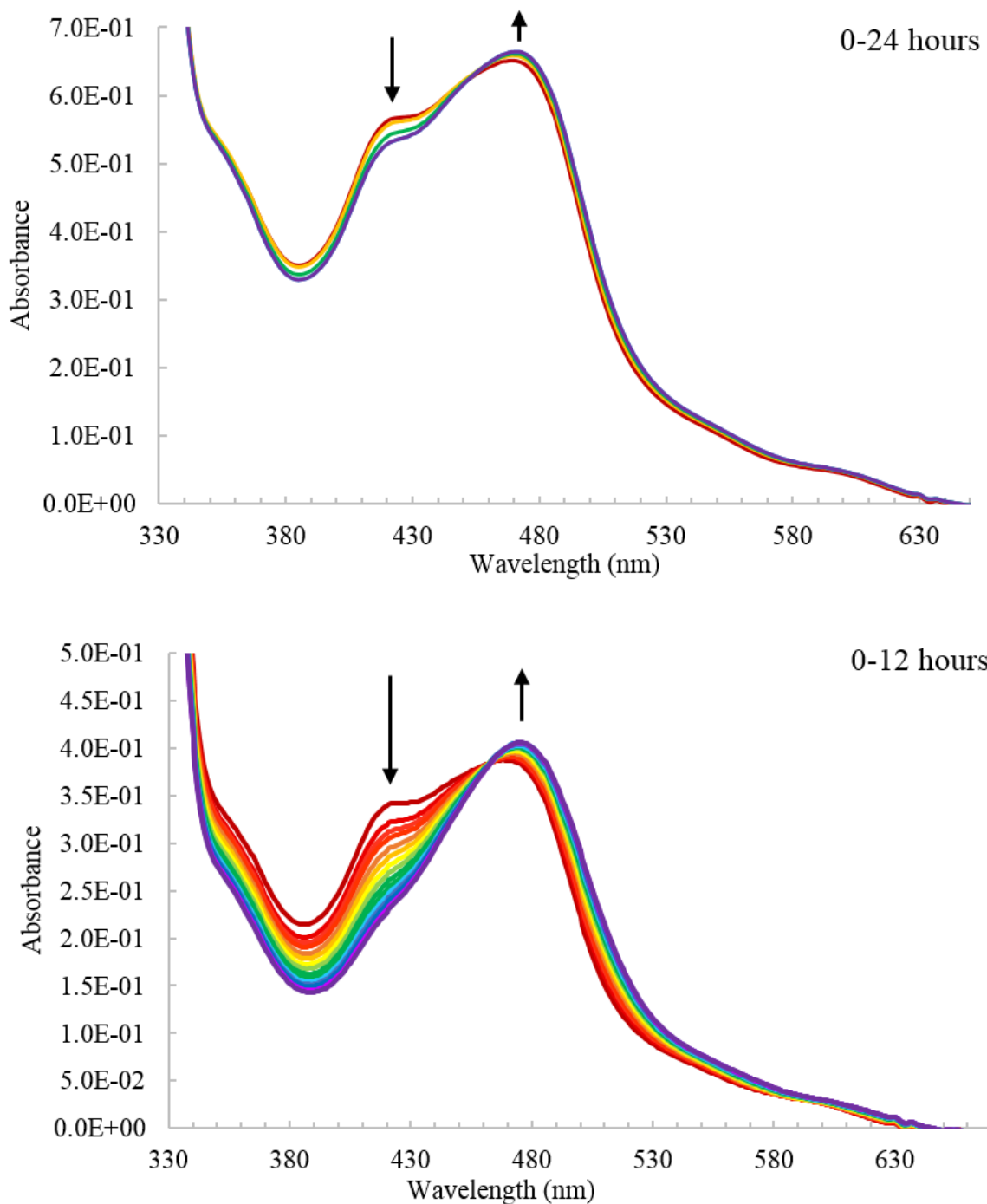


Figure 4.9 Changes to the electronic absorption spectrum of $[\text{Ru}(\text{tpy})(\text{bpy})(\text{Q})]^{2+}$ as a function of time when kept in the dark (top: 0, 1, 4, 24 hrs) and following irradiation with >395 nm light (bottom: 0 hr, 20 min, 40 min, 1 hr, 2 hrs, 3 hrs, 4 hrs, 5 hrs, 6 hrs, 7 hrs, 8 hrs, 9 hrs, 10 hrs, 11 hrs, 12 hrs) in water.

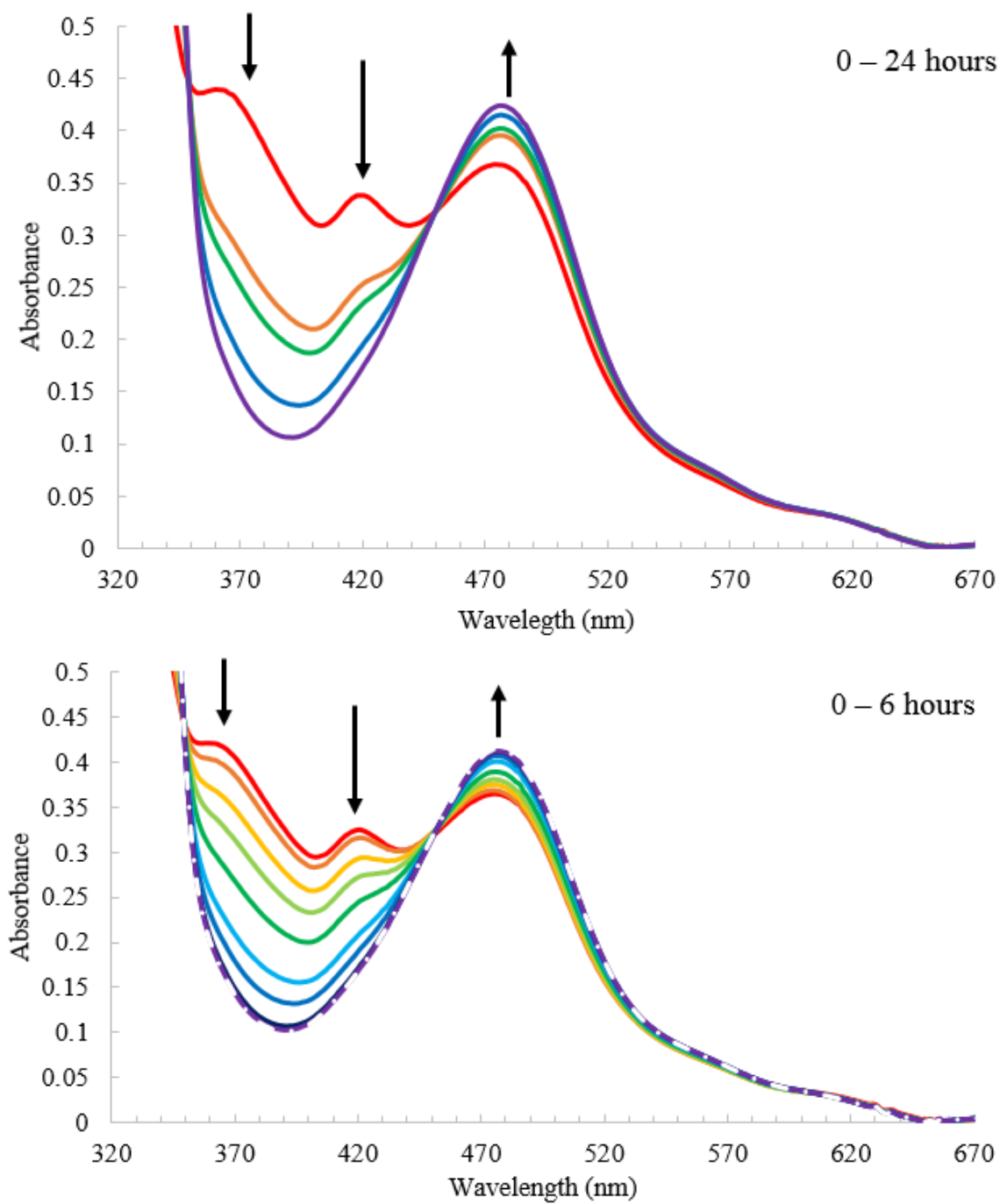


Figure 4.10 Changes to the electronic absorption spectrum of $[\text{Ru}(\text{tpy})(\text{bpy})(\text{CQ})]^{2+}$ as a function of time when kept in the dark (top: 0 hrs, 2 hrs, 3 hrs, 6 hrs, 24 hrs) and following irradiation with >395 nm light (bottom: 0 mins, 1 min, 5 mins, 10 mins, 20 mins, 40 mins, 60 mins, 120 mins, 6 hrs) in water.

Chapter 5: Conclusion

Ideally the new PCT complexes should be dark stable in water, and other aqueous and cell media, exhibit photoreactivity causing ligand release when irradiated, and possess large dissociative quantum yields at low energy wavelengths. All three of these properties are essential for the novel mode of drug delivery to be considered efficient and viable to be used as a new form of treatment. The new complexes $[\text{Ru}(\text{tpy})(\text{bpy})(\text{Q})]^{2+}$ and $[\text{Ru}(\text{tpy})(\text{bpy})(\text{CQ})]^{2+}$ were synthesized, isolated, and later characterized using ESI mass spectra and a combination of 1D and 2D NMR spectroscopies. They have proven to be both dark stable and to undergo photoinduced ligand exchange in acetonitrile upon irradiation, exhibit ϵ values of approximately $8000 \text{ M}^{-1}\text{cm}^{-1}$ and $7100 \text{ M}^{-1}\text{cm}^{-1}$ for the control compound and drug bound complex at their respective $^1\text{MLCT}$ absorption maxima, and possess small quantum yield values, ϕ_{500} , 0.00028(4) and 0.00032(3), respectively, in acetonitrile. The very inefficient drug release was expected for these complexes due to the lack of steric strain usually provided by the bidentate ligand, as previously reported for related experiments involving $[\text{Ru}(\text{tpy})(\text{NN})(\text{py})]^{2+}$ type compounds.^{32,33,35} The addition of bulky groups to the bidentate ligand increases sterics and distorts the pseudo octahedral geometry of the hexacoordinate metal center, resulting in more efficient dissociation and thus larger quantum yields.³²⁻³⁵ Unfortunately, when tested in water, the complexes did not exhibit dark stability, gradually dissociating in solution overtime without an irradiation

source. This finding presents a major problem as water is the main medium in which the majority of biological processes take place, and is the proposed solvent these complexes are to be administered. The inactivity of the compounds in the dark is crucial to using the drugs in targeted therapy; therefore, these complexes do not meet the minimum requirements needed to be effective PDT agents.

Although chloroquine has proven to be an unsuccessful candidate for photo induced ligand dissociation for the proposed treatment of cutaneous Leishmaniasis, in future studies other non-quinoline based drugs may prove to be more aqua stable. Additionally, this method of targeted treatment can be applied to other topical diseases and ailments outside Leishmaniasis, such as fungal infections and skin cancers.

References

- (1) Ferlay, J.; Bray, F.; Pisani, P.; Parkin, D. *GLOBOCAN 2002: Cancer incidence, mortality and prevalence worldwide*; 2004; Vol. 5.
- (2) Dasari, S.; Bernard Tchounwou, P. *European Journal of Pharmacology*. 2014, pp 364–378.
- (3) Gelasco, A.; Lippard, S. J. *Biochemistry* **1998**, 37 (26), 9230–9239.
- (4) Dunham, Shari U.; Dunham, Stephen U.; Gelasco, Andrew; Ishibashi, Toru; Marla, Sudhakar S.; Ohndorf, Uta-Maria; Sandman, Karen E.; Zamble, Deborah B.; Lippard, S. J. *B. Abstr. 216th ACS Natl. Meet. Boston, August 23-27* **1998**.
- (5) Cohen, S. M.; Mikata, Y.; He, Q.; Lippard, S. J. *Biochemistry* **2000**, 39 (38), 11771–11776.
- (6) Johnstone, T. C.; Suntharalingam, K.; Lippard, S. J. *Philos. Trans. R. Soc. A Math. Phys. Eng. Sci.* **2015**, 373 (2037), 20140185–20140185.
- (7) Stingele, J.; Habermann, B.; Jentsch, S. *Trends in Biochemical Sciences*. 2015, pp 67–71.
- (8) Cero-Carrasco, J.; Jacquemin, D.; Caue, E. *Phys. Chem.* **2012**, 14 (14), 12457–12464.
- (9) Alhadeff, A. L.; Holland, R. A.; Nelson, A.; Grill, H. J.; De Jonghe, B. C. *J. Neurosci.* **2015**, 35 (31), 11094–11104.

- (10) Santabarbara, G.; Maione, P.; Rossi, A.; Gridelli, C. *Expert Opin. Pharmacother.* **2016**, *17* (4), 561–570.
- (11) Rajapakse, C. S. K.; Martínez, A.; Naoulou, B.; Jarzecki, A. A.; Suárez, L.; Deregnaucourt, C.; Sinou, V.; Schrével, J.; Musi, E.; Ambrosini, G.; Schwartz, G. K.; Sánchez-Delgado, R. A. *Inorg. Chem.* **2009**, *48* (3), 1122–1131.
- (12) Bellnier, D. A.; Greco, W. R.; Loewen, G. M.; Nava, H.; Oseroff, A. B.; Dougherty, T. J. *Lasers Surg. Med.* **2006**, *38* (5), 439–444.
- (13) Kuo, W. J.; Wang, Y. C.; Chen, M. H.; Tung, F. I.; Liu, T. Y. *Ceram. Int.* **2017**, *43*, S789–S796.
- (14) Smits, T.; Moor, A. C. E. *Journal of Photochemistry and Photobiology B: Biology.* 2009, pp 159–169.
- (15) Dennis E.J.G.J. Dolmans, D. F. and R. K. J. *Nat. Rev. - Cancer* **2003**, *3*, 380–387.
- (16) DUSA Pharmaceuticals, I. *Pharm. database* **1999**.
- (17) Mustafa, F. H.; Jaafar, M. S. *Indian J. Phys.* **2013**, *87* (3), 203–209.
- (18) Federal Drug Administration; Cder. *Pharm. database* **1995**.
- (19) Diffey, B. *Phys. Med. Biol* **1980**, *25*, 405–426.
- (20) Thompson, C.; Stinson, D.; Smith, A. *Lancet* **1990**, *336* (8717), 703–706.
- (21) Mamalis, A.; Koo, E.; Garcha, M.; Murphy, W. J.; Isseroff, R. R.; Jagdeo, J. J. *Biophotonics* **2016**, *9* (11–12), 1167–1179.
- (22) Susan Pei, A. C. I.; Keshavmurthy A. Adya²; Maria M. Tsoukas¹. *Indian Dermatology Online J. -May* **2015**, *6* (3), 145–157.
- (23) Liu, W.; Xin, Y. *Baotou Med. Coll.* **2016**, *32* (7), 64–65.

- (24) Arden, G. B.; Sivaprasad, @bullet S. *Doc. Ophthalmol* **2012**, *124*, 15–26.
- (25) Sivaprasad, S.; Arden, G. *Eye* **2016**, *30*, 189–192.
- (26) Miranda, N.; Volpato, H.; Da, J. H.; Rodrigues, S.; Caetano, W.; Ueda-Nakamura, T.; De Oliveira Silva, S.; Nakamura, C. V.; Henrique, J. **2017**.
- (27) Johnstone, D. M.; Moro, C.; Stone, J.; Benabid, A.-L.; Mitrofanis, J. *Front. Neurosci.* **2016**, *9*.
- (28) Kalyanasundaram, K. *Coord. Chem. Rev.* **1982**, *46* (C), 159–244.
- (29) Kalyanasundaram, K.; Graetzel, M. *Curr. Opin. Biotechnol.* **2010**, *21* (3), 298–310.
- (30) Lo, K. K.-W.; Li, S. P.-Y. *RSC Adv.* **2014**, *4* (21), 10560.
- (31) Anderson, B. L.; Maher, A. G.; Nava, M.; Lopez, N.; Cummins, C. C.; Nocera, D. *G. J. Phys. Chem. B* **2015**, *119* (24), 7422–7429.
- (32) Knoll, J. D.; Albani, B. A.; Turro, C. *Acc. Chem. Res.* **2015**, *48* (8), 2280–2287.
- (33) Loftus, L. M.; White, J. K.; Albani, B. A.; Kohler, L.; Kodanko, J. J.; Thummel, R. P.; Dunbar, K. R.; Turro, C. *Chem. - A Eur. J.* **2016**, *22* (11), 3704–3708.
- (34) Knoll, J. D.; Albani, B. A.; Turro, C. *Chem. Commun.* **2015**, *51* (42), 8777–8780.
- (35) Knoll, J. D.; Albani, B. A.; Durr, C. B.; Turro, C. *J. Phys. Chem. A* **2014**, *118* (45), 10603–10610.
- (36) Juris, A.; Balzani, V.; Barigelletti, F.; Campagna, S.; Belser, P.; von Zelewsky, A. *Coord. Chem. Rev.* **1988**, *84* (C), 85–277.
- (37) Demas, J. N.; Adamson, A. W. *J. Am. Chem. Soc.* **1971**, *93*, 1800–1801.
- (38) Colasson, B.; Credi, A.; Ragazzon, G. *Coordination Chemistry Reviews.* 2016, pp

125–134.

- (39) Thota, S.; Vallala, S.; Yerra, R.; Rodrigues, D. A.; Raghavendra, N. M.; Barreiro, E. J. *Int. J. Biol. Macromol.* **2016**, *82*, 663–670.
- (40) Chen, Y.; Luo, X.; Bai, L.; Hu, X.; Zhou, J.; Zhang, P.; Yu, Y. *New J. Chem. New J. Chem* **2017**, *41* (41), 10225–10230.
- (41) Novakova, O.; Kasparkova, J.; Bursova, V.; Hofr, C.; Vojtiskova, M.; Chen, H.; Sadler, P. J.; Brabec, V. *Chem. Biol.* **2005**, *12* (1), 121–129.
- (42) Colina-Vegas, L.; Villarreal, W.; Navarro, M.; De Oliveira, C. R.; Graminha, A. E.; Maia, P. I. D. S.; Deflon, V. M.; Ferreira, A. G.; Cominetti, M. R.; Batista, A. *J. Inorg. Biochem.* **2015**, *153*, 150–161.
- (43) Liu, X. W.; Lu, J. L.; Chen, Y. D.; Li, L.; Zhang, D. S. *Inorganica Chim. Acta* **2011**, *379* (1), 1–6.
- (44) Sainuddin, T.; McCain, J.; Pinto, M.; Yin, H.; Gibson, J.; Hetu, M.; McFarland, S. A. *Inorg. Chem.* **2016**, *55* (1), 83–95.
- (45) Liu, Y.; Hammitt, R.; Lutterman, D. A.; Joyce, L. E.; Thummel, R. P.; Turro, C. *Inorg. Chem.* **2009**, *48* (1), 375–385.
- (46) Eales, K. L.; Hollinshead, K. E. R.; Tennant, D. A. *Oncogenesis* **2016**, *5* (1), e190.
- (47) Unjaroen, D.; Chen, J.; Otten, E.; Browne, W. R. *Inorg. Chem.* **2017**, *56* (2), 900–907.
- (48) Sánchez-Delgado, R. A.; Navarro, M.; Pérez, H.; Urbina, J. A. *J. Med. Chem.* **1996**, *39* (5), 5204–5209.
- (49) Iniguez, E.; Sánchez, A.; Vasquez, M. A.; Martínez, A.; Olivas, J.; Sattler, A.;

- Sánchez-Delgado, R. A.; Maldonado, R. A. *J. Biol. Inorg. Chem.* **2013**, *18* (7), 779–790.
- (50) Giarolla, J.; Ferreira, E. I. *Mini-Reviews Med. Chem.* **2015**, *15* (3), 220–242.
- (51) D ’annessa, I.; Castelli, S.; Desideri, A. *Mini-Reviews Med. Chem.* **2015**, *15* (3), 203–210.
- (52) de Paiva-Cavalcanti, M.; de Moraes, R. C. S.; Pessoa-E-Silva, R.; Trajano-Silva, L. A. M.; Gonçalves-de-Albuquerque, S. da C.; Tavares, D. de H. C.; Brelaz-de-Castro, M. C. A.; Silva, R. de F. E.; Pereira, V. R. A. *Cell Biosci.* **2015**, *5*, 31.
- (53) Gupta, G.; Oghumu, S.; Satoskar, A. R. *Adv. Appl. Microbiol.* **2013**, *82*, 155–184.
- (54) Giudice, A.; Vendrame, C.; Bezerra, C.; Carvalho, L. P.; Delavechia, T.; Carvalho, E. M.; Bacellar, O. *BMC Infect. Dis.* **2012**, *12* (1), 75.
- (55) Teixeira, C.; Vale, N.; Pérez, B.; Gomes, A.; Gomes, J. R. B.; Gomes, P. *Chemical Reviews*. 2014, pp 11164–11220.
- (56) Rendal, C.; Kusk, K. O.; Trapp, S. *Environ. Toxicol. Chem.* **2011**, *30* (2), 354–359.
- (57) Slater, A. F. G. *Pharmac. Ther* **1993**, *57*, 203–235.
- (58) Golden, E. B.; Cho, H.-Y.; Hofman, F. M.; Louie, S. G.; Schönthal, A. H.; Chen, T. C. *Neurosurg. Focus* **2015**, *38* (3), E12.
- (59) Hoekenga, M. T. *J Am Med Assoc* **1952**, *149* (15), 1369–1371.
- (60) Bawa, S.; Kumar, S.; Drabu, S.; Kumar, R. *J. Pharm. Bioallied Sci.* **2010**, *2* (2), 64–71.
- (61) Sullivan, B. P.; Calvert, J. M.; Meyer, T. J. *Inorg. Chem.* **1980**, *198646* (901415), 1404–1407.

- (62) Takeuchi, K. J.; Thompson, M. S.; Pipes, D. W.; Meyer, T. J. *Inorg. Chem. J. Chem. Phys* **1984**, *23* (63), 1845–1851.
- (63) Ho, M. Y.; Chiou, M. L.; Du, W. S.; Chang, F. Y.; Chen, Y. H.; Weng, Y. J.; Cheng, C. C. *J. Inorg. Biochem.* **2011**, *105* (6), 902–910.
- (64) Wasylenko, D. J.; Ganesamoorthy, C.; Koivisto, B. D.; Berlinguette, C. P. *Eur. J. Inorg. Chem.* **2010**, *2010* (20), 3135–3142.
- (65) Hecker, C. R.; Fanwick, P. E.; McMillin, D. R. *Inorg. Chem.* **1991**, *30* (4), 659–666.
- (66) Murov, S. L.; Carmichael, I.; Hug, G. L. *Handbook of Photochemistry, Second Edition*, 2nd ed.; Marcel Dekker, Inc.: New York, 1993.
- (67) Pietrzak, M.; Dobkowski, J. *J. Am. Chem. Soc* **2002**, *124* (1).
- (68) Tsai, C.; Allard, M. M.; Lord, R. L.; Luo, D.; Chen, Y.; Schlegel, H. B.; Endicott, J. F. *Inorg. Chem.* **2011**, *50*, 11965–11977.
- (69) Tsai, C.; Allard, M. M.; Lord, R. L.; Luo, D.; Chen, Y.; Schlegel, H. B.; Endicott, J. F. No. ii.